https://doi.org/10.5194/egusphere-2026-6846
Preprint. Discussion started: 12 November 2026
© Author(s) 2026. CC BY 4.0 License.

Motion compensation and sensor time synchronization for Doppler wind LIDAR on an uncrewed lightship

Pascal Guillouët[1], Astrid Lampert[1], and Beatriz Cañadillas[1]

[1]Institute of Flight Guidance, TU Braunschweig, Hermann-Blenk-Str. 27, 38108 Braunschweig, Germany

Correspondence: Beatriz Cañadillas (b.canadillas@tu-braunschweig.de)

Abstract. Platform motion can distort the beam geometry and introduce errors into radial velocity measurements from floating Doppler wind LIDAR (Light Detection and Ranging) systems. Building on an earlier assessment of lightship-based wind measurements, this study investigates retrospective time synchronization between sensors and motion compensation for a wind LIDAR installed on an uncrewed lightship in the German Bight. Global Positioning System (GPS) and attitude and heading reference system (AHRS) measurements are combined with LIDAR radial velocities to correct for platform motion, interpolate observations to nominal heights, and reconstruct wind vectors using a least-squares solution based on five lines of sight (LOS). A time-shift optimization based on the mean sum of squared residuals (SSR) estimates hourly time offsets between the LIDAR and motion-data data, providing a post-processing synchronization approach that could be applied to other Doppler wind LIDAR systems equipped with suitable motion-sensors. Post-processing reduced the variability of high-frequency wind speed estimates, while its effect on the 10-minute mean horizontal wind speed remained small: mean corrected-minus-raw differences ranged from $-0.037\,\mathrm{m\,s^{-1}}$ to $-0.028\,\mathrm{m\,s^{-1}}$ in three evaluated heights. The small effect on the mean wind speed is consistent with the finding of Cañadillas et al. (2026), who analysed measurements over a longer period. LIDAR-derived turbulence intensity decreased by approximately 0.03 to 0.04 in absolute terms, although the contributions of motion compensation and wind-vector-reconstruction choices were not isolated. A simple correction based on the 10-minute mean platform heading yielded 10-minute wind directions close to those obtained with full motion compensation, with standard deviation differences below $0.71°$. These findings support the practical use of this heading-based correction to obtain geographically referenced mean wind directions under the investigated conditions. Onboard meteorological observations provide a plausibility check for the corrected winds, but the absence of independent reference measurements at comparable heights prevents a full assessment of their accuracy. Together with the earlier assessment, this study provides a practical basis for refining the processing of lightship-based wind measurements and helps future users of the planned open-access dataset select correction methods suited to their temporal scales and applications.

1 Introduction

Long-term observations of offshore wind speed and direction at multiple heights support wind-resource assessment, wind power forecasting, and evaluation of atmospheric models, among others. Their usefulness depends on the reliability of the retrieved wind profiles, which need to be assessed for the measurement technique and deployment conditions.

https://doi.org/10.5194/egusphere-2026-6846
Preprint. Discussion started: 12 November 2026
© Author(s) 2026. CC BY 4.0 License.

Meteorological masts provide wind measurements at fixed heights, but offshore installations are expensive to construct and maintain. In the German Bight, the *FINO1* and *FINO3* offshore research platforms provide such observations alongside a broader range of meteorological and oceanographic measurements (BSH, Bundesamt für Seeschifffahrt und Hydrographie). Doppler wind LIDAR (light detection and ranging) systems complement these observations by extending wind measurements to greater heights and additional locations. However, they cannot fully replace instrumented meteorological masts, as they do not independently provide, for instance, the temperature and humidity profiles needed to characterize atmospheric stratification. Deployments at multiple locations can help to better characterize the spatial variations in the offshore wind field, particularly in regions such as the North Sea, where operating wind farms modify the surrounding flow through wakes and wind-farm cluster effects (Cañadillas et al., 2020; Platis et al., 2018).

Doppler wind LIDAR systems provide a cost-effective alternative by measuring three-dimensional wind vectors using laser-based Doppler techniques, allowing simultaneous measurements at multiple heights from a single instrument. While widely used on fixed platforms, the deployment of wind LIDARs on floating platforms, such as buoys, introduces additional challenges, as platform motion can distort the measurement geometry and degrade the accuracy of the retrieved wind vectors (Lang and McKeogh, 2011; Pichugina et al., 2012; Peña et al., 2015; IEC61400-50-4, 2025).

Considerable effort has been devoted to understanding and compensating for the effects of platform motion on floating-LIDAR system (FLS) measurements, and a variety of compensation approaches have been proposed, including active platform control (Pichugina et al., 2012; Tiana-Alsina et al., 2015) or post-processing algorithms (Gutiérrez et al., 2015), often using inertial and Global Positioning System (GPS) measurements of the platform motion (Cañadillas et al., 2026; Gottschall et al., 2014; Yamaguchi and Ishihara, 2016; Gutiérrez-Antuñano et al., 2018; Kelberlau et al., 2020; Désert et al., 2021; Benzo et al., 2024). These approaches have generally been shown to improve the accuracy of retrieved wind vectors. However, because platform dynamics vary considerably between different floating-platform concepts, the necessity and effectiveness of motion-compensation algorithms should be evaluated for each specific application.

As part of the *FINO1 – Meteorologische Messungen* project (TUBS), an uncrewed lightship equipped with meteorological instruments, including a vertical pulsed wind LIDAR, was deployed in the German Bight. Its motion characteristics differ from those of conventional buoy-based FLS because of its size, mass, and mooring configuration. Previous work showed that platform motion can affect the LIDAR measurement geometry, particularly under rough sea conditions. That study reported generally small differences between corrected and uncorrected 10-minute mean wind speeds and highlighted the importance of accounting for the vessel's heading to obtain geographically referenced wind directions (Cañadillas et al., 2026).

Building on these findings, the present study investigates the motion-correction procedure in greater detail by focusing on the effects on high-frequency measurements used during the correction process. Particular emphasis is placed on the retrospective time synchronization of the LIDAR, GPS, and attitude and heading reference system (AHRS) measurements. An optimization procedure based on the sum of squared residuals (SSR) retrieved during a least-squares wind vector reconstruction is introduced to improve the temporal alignment of the different sensors. Therefore, a refined wind-vector reconstruction is first developed, involving compensation for effects of rotational and translational platform motion. Finally, the combined synchronization and post-processing procedure is evaluated using measurements collected during November 2021, focusing on its effects on

https://doi.org/10.5194/egusphere-2026-6846
Preprint. Discussion started: 12 November 2026
© Author(s) 2026. CC BY 4.0 License.

high-frequency and 10-minute wind estimates and their variability. Comparisons with conventional onboard meteorological observations provide a plausibility check of the corrected wind conditions.

The remainder of this paper is organized as follows. Section 2 describes the measurement platform and introduces the proposed motion-compensation methodology, with particular emphasis on the retrospective time synchronization of the LIDAR and motion data. Section 3 evaluates the proposed approach using measurements collected under different environmental conditions. Finally, the results are discussed, and the main conclusions are summarized in Sect. 4.

2 Materials and methods

This section first introduces the measurement setup and sensors used in this study. It then describes the wind LIDAR measurement principle for a fixed installation, briefly examines the potential effects of platform motion, and presents the post-processing algorithm for motion compensation. Finally, a method is proposed to improve the retrospective synchronization of LIDAR and motion-sensor data.

2.1 Site and instrumentation

The experimental platform used in this study is the uncrewed lightship *UFS4* (Fig. 1), which is operated by the *Wasserstraßen- und Schifffahrtsamt Weser-Jade-Nordsee*. Stationed in the German Bight as a navigational aid, the lightship is equipped with a Leosphere WindCube v2® pulsed Doppler LIDAR (yellow box in Fig. 1) for continuous measurements of vertical wind profiles. The ship's motion is tracked using a dedicated Magellan Professional 3011® dual GPS receiver together with a Microstrain 3DM-GX3-35® AHRS, consisting of an inertial measurement unit (IMU), a magnetometer, and an internal GPS receiver. While the AHRS is installed within the same yellow box as the wind LIDAR (Fig. 1), the dedicated GPS receiver is mounted on the exterior deck, in close proximity to the remaining sensors. The deck is located approximately $5.5\,\mathrm{m}$ above the sea surface. Furthermore, the ship serves as an automated weather station for the German Meteorological Service (*Deutscher Wetterdienst*, DWD) and is therefore equipped with several other meteorological instruments, including a cup anemometer and a wind vane on top of the ship's mast (approximately $14\,\mathrm{m}$ above the sea surface). The analysis presented in the following sections is based on measurements collected during November 2021. During this period, the lightship was stationed approximately $80\,\mathrm{km}$ off the Dutch coast near Groningen at $54°10′5.80″\,\mathrm{N}$, $6°20′48.64″\,\mathrm{E}$.

2.2 WindCube v2 measurement principle

The WindCube v2 is a pulsed Doppler wind LIDAR that determines radial wind velocities along a line of sight (LOS) from the measured Doppler shift of laser light which is backscattered by atmospheric aerosols. Owing to its pulsed measurement principle, radial wind velocities are obtained simultaneously at multiple predefined nominal heights along the laser beam by assigning the time of received signals to different range gates. Since a single LOS measurement provides only the wind-velocity component parallel to the beam direction, at least three linearly independent LOS directions are required to reconstruct

https://doi.org/10.5194/egusphere-2026-6846
Preprint. Discussion started: 12 November 2026
© Author(s) 2026. CC BY 4.0 License.



Figure 1. The uncrewed lightship *UFS4* with the deck-mounted WindCube v2 pulsed Doppler LIDAR. The inset shows the LIDAR enclosure, and the overlaid schematic illustrates the four inclined beams and the vertical beam. The indicated dimensions show the ship length (26 m) and the approximate mast-top height above the sea surface (14 m). Reproduced from Cañadillas et al. (2026).

the three-dimensional wind vector

$$\mathbf{V}_{\mathrm{wind}}(h) = \begin{pmatrix} u(h) \\ v(h) \\ w(h) \end{pmatrix} \tag{1}$$

at a nominal height h from the LIDAR's position. For this purpose, the WindCube v2 employs the Doppler beam swinging (DBS) technique, where a single laser beam is successively steered into multiple different LOS (Fig. 2), assuming that the wind field is spatially homogeneous and remains approximately stationary during the scan. A detailed description of the instrument and its internal reconstruction algorithm is provided in Désert et al. (2021); Pauliac (2009). Only the aspects relevant to the present study are summarized below.

https://doi.org/10.5194/egusphere-2026-6846
Preprint. Discussion started: 12 November 2026
© Author(s) 2026. CC BY 4.0 License.

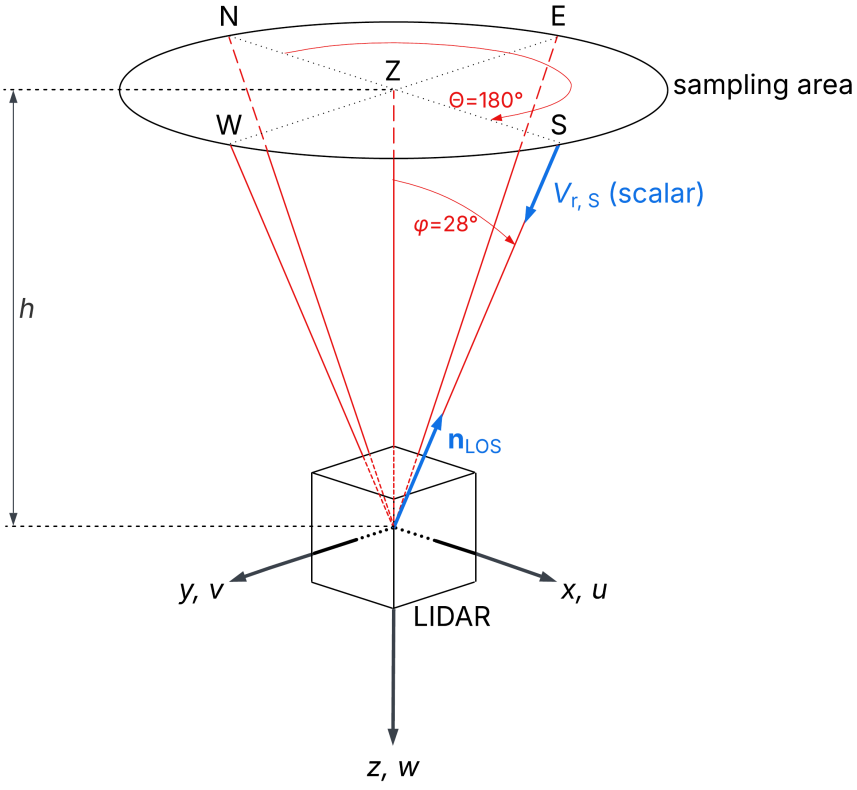


Figure 2. WindCube v2 internal reference frame and beam geometry in relation to the cardinal directions, when installed correctly following the instructions (Pauliac, 2009). h denotes a predefined nominal height. The azimuth angle Θ and zenith angle φ are displayed exemplarily for the beam directed toward the South. $\mathbf{n}_{\mathrm{LOS}}$ denotes the unit vector pointing toward the beam direction and $V_{\mathrm{r,S}}$ is the respective radial component of the underlying wind vector, defined positive toward the LIDAR.

The WindCube v2 employs five different LOS, each defined by an azimuth angle Θ and a zenith angle φ (see Fig. 2). Using the *South, West, Down (SWD)* WindCube reference frame shown in Fig. 2, each LOS can be represented by a unit vector pointing away from the LIDAR toward the LOS direction:

$$\mathbf{n}_{\mathrm{LOS}} = \begin{pmatrix} -\cos\Theta\sin\varphi \\ -\sin\Theta\sin\varphi \\ -\cos\varphi \end{pmatrix} \tag{2}$$

The measured radial wind velocity V_{r} is defined as positive in the opposite direction to $\mathbf{n}_{\mathrm{LOS}}$, meaning it can be expressed as a projection of the true wind vector at the measurement height h onto the negative LOS unit vector:

$$V_{\mathrm{r}}(h) = \mathbf{V}_{\mathrm{wind}}(h) \cdot (-\mathbf{n}_{\mathrm{LOS}}) = u(h)\cos\Theta\sin\varphi + v(h)\sin\Theta\sin\varphi + w(h)\cos\varphi. \tag{3}$$

https://doi.org/10.5194/egusphere-2026-6846
Preprint. Discussion started: 12 November 2026
© Author(s) 2026. CC BY 4.0 License.

In a usual, fixed setup, the WindCube v2 uses four inclined beams (indices N, E, S, W) with a zenith angle of $\varphi = 28°$, pointing toward the instrument-relative cardinal directions ($\Theta = 0°,\ 90°,\ 180°,\ 270°$), followed by a vertical beam (index Z) defined by $\varphi = 0°$ (see Fig. 2). The laser emitter repeatedly steers the beam into those LOS positions successively in the mentioned order. The wind-vector components are then reconstructed by the device at each time step (i.e. after each new LOS measurement) by using the latest five radial velocities:

$$u(h) = \frac{V_{\mathrm{r,N}}(h) - V_{\mathrm{r,S}}(h)}{2\sin\varphi}, \tag{4}$$

$$v(h) = \frac{V_{\mathrm{r,E}}(h) - V_{\mathrm{r,W}}(h)}{2\sin\varphi}, \tag{5}$$

$$w(h) = V_{\mathrm{r,Z}}(h). \tag{6}$$

Note that the components are defined according to the LIDAR reference frame, leading to u pointing to the South, v to the West and w pointing downward. From the reconstructed wind-vector components, the horizontal wind speed V and the wind direction D are derived as

$$V(h) = \sqrt{u(h)^2 + v(h)^2}, \tag{7}$$

$$D(h) = 180° + \arctan2\left[-v(h), -u(h)\right]. \tag{8}$$

Here, D denotes the direction from which the wind blows. Due to the conical beam geometry, measurements at a given height are not obtained at a single point but over a horizontal sampling area. The spatial extent of this area increases with h, thereby limiting the resolution of small-scale flow structures and making the assumption of horizontally homogeneous flow progressively less valid.

The WindCube v2 used in this study operates with an update frequency of approximately 1 Hz. With 20 000 pulses per LOS and a pulse repetition frequency of 30 000 Hz, the accumulation time of the backscattered signals per LOS is 0.667 s. Including transition times, a full DBS scan over all five beam directions takes about 4.2 s. A new wind vector is retrieved after each LOS measurement using the latest measurement from each of the five beam directions; two consecutive wind vectors therefore share four of their underlying LOS measurements. The WindCube provides the high-frequency realtime wind vectors $\mathbf{V}_{\mathrm{wind}}(h)$ together with the latest measured radial velocities $V_{\mathrm{r}}(h)$ for each LOS and range-gate measurement, as well as standard 10-minute statistical products.

2.3 Post-processing of high-frequency LIDAR wind data

With a floating-LIDAR system (FLS) application, the LIDAR is installed on a moving platform, thereby introducing six new degrees of freedom to the measurement system. Owing to the DBS technique, the LIDAR acquires radial information about the wind field along different LOS successively rather than simultaneously, allowing the platform to change its position and orientation between individual measurements, particularly under rough sea conditions. Consequently, each LOS measurement is affected by a different platform state, resulting in motion-dependent distortions of the reconstructed wind vectors.

https://doi.org/10.5194/egusphere-2026-6846
Preprint. Discussion started: 12 November 2026
© Author(s) 2026. CC BY 4.0 License.

Pure translational motion alone barely affects the DBS geometry of the LIDAR, but it directly distorts the measured radial velocity V_r, as a moving device experiences a change in the backscattered signal's Doppler shift compared to a device that is fixed in place. Furthermore, translational movement leads to a change in the measurement position. Horizontal position changes are assumed to be negligible for the present application, whereas a vertical displacement may introduce errors owing to the vertical gradients in the wind field. Rotational platform motion alters the DBS geometry assumed by the internal WindCube reconstruction algorithm. More specifically, the azimuth angle Θ and the zenith angle φ of each LOS measurement vary according to the instantaneous platform attitude, causing each LOS to deviate from its nominal orientation. Since the internal reconstruction algorithm assumes fixed beam orientation, the resulting wind vectors are reconstructed using incorrect DBS geometries, introducing errors into both the horizontal wind speed and wind direction. In addition, changes in the zenith angle φ also modify the effective measurement height h of each radial observation, introducing further errors due to the vertical gradients in the wind field.

Consequently, each LOS measurement has to be corrected individually, taking into account the underlying conditions under the influence of platform motion at the time of the measurement. For the exact measurement setup used for this study, Cañadillas et al. (2026) introduced a post-processing algorithm that transforms the LOS geometry into an Earth-fixed reference frame and accounts for motion-induced changes in measurement height. Building on this work, the present study uses a five-LOS least-squares reconstruction of wind vectors based on the motion-corrected radial velocities and introduces a new retrospective time-synchronization procedure for the LIDAR and platform-motion measurements.

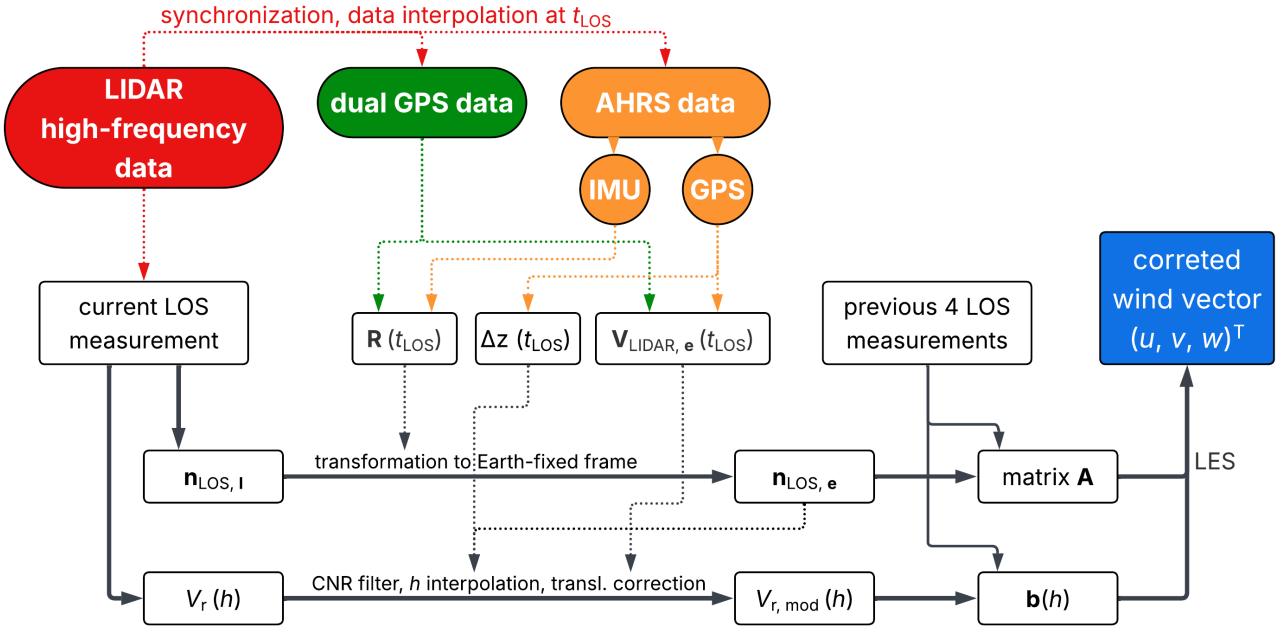


Figure 3. Diagram of the LIDAR high-frequency data post-processing logic.

https://doi.org/10.5194/egusphere-2026-6846
Preprint. Discussion started: 12 November 2026
© Author(s) 2026. CC BY 4.0 License.

In order to correct the LIDAR high-frequency wind vectors, instead of applying Eq. 4–6 directly to the measured radial velocities, we use a linear equation system (LES) based on Eq. 3 to reconstruct a motion-compensated wind vector for each time step, taking into account the LIDAR's orientation and linear motion. An overview of the modified high-frequency wind-vector reconstruction is shown in Fig. 3. Following the internal WindCube v2 logic, each wind vector $\mathbf{V}_{\mathrm{wind}}(h)$ integrates the information obtained from the latest five LOS measurements, leading to an overdetermined 5x3 LES of the following form:

$$\mathbf{A} \cdot \mathbf{V}_{\mathrm{wind}}(h) = \mathbf{b}(h) \tag{9}$$

The matrix $\mathbf{A}$ consists of the negative unit vectors $\mathbf{n}_{\mathrm{LOS,e}}$ from the respective LOS measurements, each representing the true direction of the laser beam in an Earth-fixed reference frame:

$$\mathbf{A} = \begin{pmatrix} -\mathbf{n}_{\mathrm{LOS},1,\mathbf{e}}^{\top} \\ -\mathbf{n}_{\mathrm{LOS},2,\mathbf{e}}^{\top} \\ -\mathbf{n}_{\mathrm{LOS},3,\mathbf{e}}^{\top} \\ -\mathbf{n}_{\mathrm{LOS},4,\mathbf{e}}^{\top} \\ -\mathbf{n}_{\mathrm{LOS},5,\mathbf{e}}^{\top} \end{pmatrix} \tag{10}$$

The unit vectors are therefore first transformed from the local LIDAR reference frame (index $\mathbf{l}$) into the Earth-fixed reference frame (index $\mathbf{e}$), according to the equation

$$\mathbf{n}_{\mathrm{LOS,e}} = \mathbf{R}(\psi, \theta, \phi) \cdot \mathbf{n}_{\mathrm{LOS,l}} \tag{11}$$

with the rotational matrix

$$\mathbf{R} = \begin{pmatrix} \cos\psi\cos\theta & \cos\psi\sin\theta\sin\phi - \sin\psi\cos\phi & \cos\psi\sin\theta\cos\phi + \sin\psi\sin\phi \\ \sin\psi\cos\theta & \sin\psi\sin\theta\sin\phi + \cos\psi\cos\phi & \sin\psi\sin\theta\cos\phi - \cos\psi\sin\phi \\ -\sin\theta & \cos\theta\sin\phi & \cos\theta\cos\phi \end{pmatrix}. \tag{12}$$

Here, the Euler angles ψ, θ, and ϕ denote the yaw, pitch, and roll angles of the LIDAR, respectively. They are defined as right-handed rotations along the $z-$, $y-$ and x-axes respectively, as shown in Fig. 4. Note that for simplicity of calculations, a rather unconventional Earth-fixed frame is used here, defined in accordance with the internal WindCube frame as *SWD*. As the device is installed in a way that its axes coincide with the lightship's axes, the ship's Euler angles are used as the LIDAR angles accordingly.

https://doi.org/10.5194/egusphere-2026-6846
Preprint. Discussion started: 12 November 2026
© Author(s) 2026. CC BY 4.0 License.

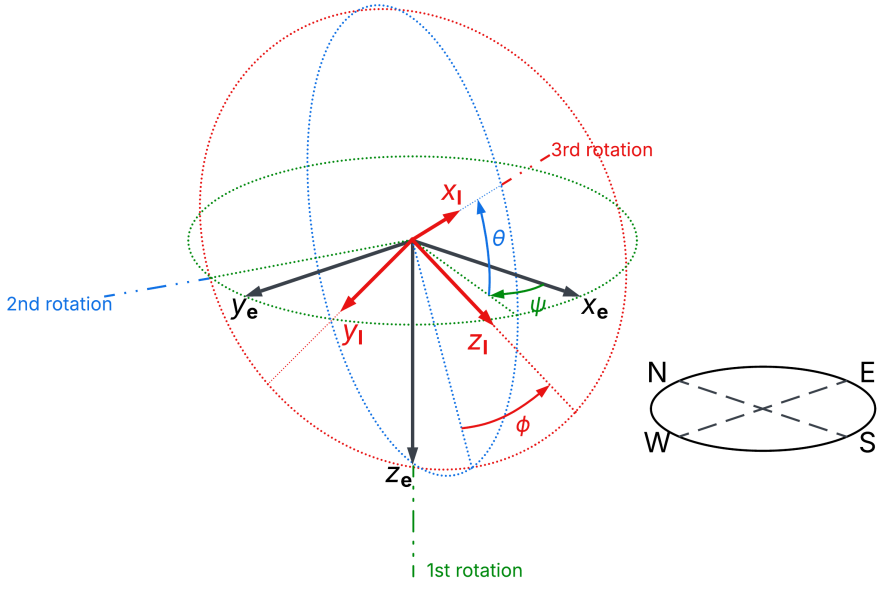


Figure 4. Euler angles (yaw ψ, pitch θ, roll ϕ), defining the orientation of the rotated LIDAR frame (index $\mathbf{l}$) with respect to the Earth-fixed frame (index $\mathbf{e}$). For a $\mathbf{l} \rightarrow \mathbf{e}$ transformation, the single rotations have to be applied in the opposite order.

The vector $\mathbf{b}(h)$ on the right side of Eq. 9 contains the modified corresponding radial velocities from the latest LOS measurements:

$$\mathbf{b}(h) = \begin{pmatrix} V_{\mathrm{r,mod},1}(h) \\ V_{\mathrm{r,mod},2}(h) \\ V_{\mathrm{r,mod},3}(h) \\ V_{\mathrm{r,mod},4}(h) \\ V_{\mathrm{r,mod},5}(h) \end{pmatrix} \tag{13}$$

Each measured radial velocity must first be modified independently to compensate for the direct effects of translational LIDAR motion and the indirect effects associated with changes in measurement height. For each raw LOS and range-gate measurement, the instantaneous measurement height h_{true} is first determined by accounting for the actual zenith angle φ_{true} of the beam and the LIDAR's current vertical offset Δz from its nominal position due to the ship's heave. Given that the z axis is defined as positive pointing downward, a positive Δz indicates a decrease in the true measurement height. Thus, h_{true} is calculated as

$$h_{\mathrm{true}} = h \cdot \cos(\varphi_{\mathrm{true}}) - \Delta z \tag{14}$$

https://doi.org/10.5194/egusphere-2026-6846
Preprint. Discussion started: 12 November 2026
© Author(s) 2026. CC BY 4.0 License.

for nominally vertical beam positions or as

$$h_{\mathrm{true}} = h \cdot \frac{\cos(\varphi_{\mathrm{true}})}{\cos(28°)} - \Delta z \tag{15}$$

for nominally inclined beams, with the true zenith angle φ_{true} obtained from the z component of the transformed unit vector:

$$\varphi_{\mathrm{true}} = \arccos(-\mathbf{n}_{\mathrm{LOS},\mathbf{e},z}). \tag{16}$$

The corresponding raw radial-velocity profiles $V_{\mathrm{r}}(h_{\mathrm{true}})$ are then mapped to the defined nominal height grid by linear interpolation, resulting in $V_{\mathrm{r,\,interp}}(h)$, as represented in Fig. 5.

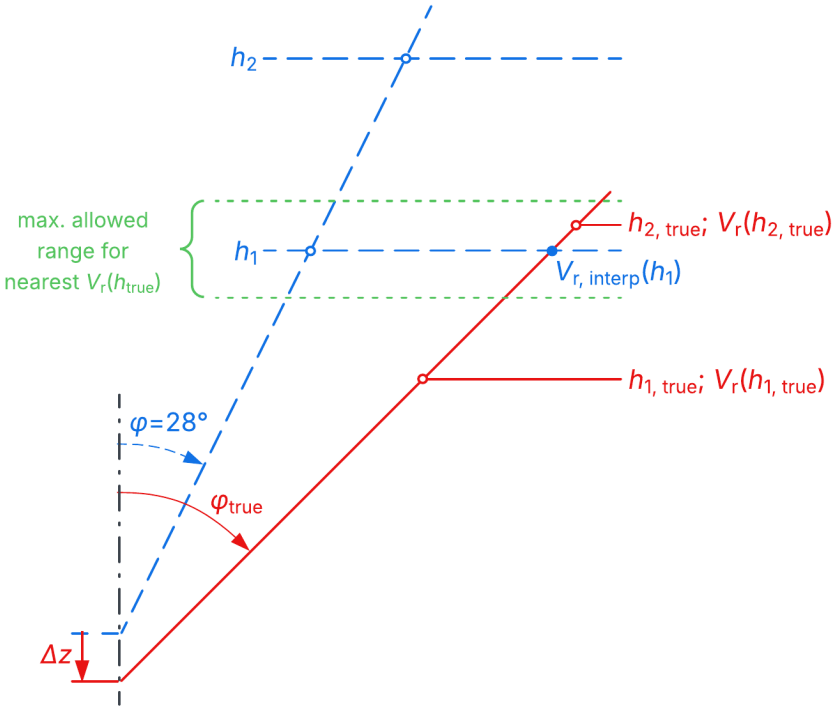


Figure 5. Sketch of the interpolated radial wind velocity $V_{\mathrm{r,\,interp}}(h)$ along an inclined beam: Mapping $V_{\mathrm{r}}(h_{\mathrm{true}})$, measured at the shifted heights h_{true}, to the grid of nominal heights h by linear interpolation. Blue dashed lines: Hypothetical, fixed LIDAR setup. Red solid lines: Altered LOS measurement geometry due to platform motion. Green dotted lines: Vertical thresholds marking the allowed range for the nearest valid raw $V_{\mathrm{r}}(h_{\mathrm{true}})$ measurement, for $V_{\mathrm{r,\,interp}}(h_1)$ to be considered valid.

During the interpolation process, two main filters are taken into account:

1. Raw $V_{\mathrm{r}}(h_{\mathrm{true}})$ measurements with a carrier-to-noise ratio (CNR) below $-23\,\mathrm{dB}$ are marked as invalid. This corresponds to an internal WindCube filtering mechanism.

https://doi.org/10.5194/egusphere-2026-6846
Preprint. Discussion started: 12 November 2026
© Author(s) 2026. CC BY 4.0 License.

2. Interpolated $V_{\mathrm{r,interp}}(h)$ values are rejected if there is no valid raw $V_{\mathrm{r}}(h_{\mathrm{true}})$ measurement available within the range $h \pm 10\,\mathrm{m}$. This filtering method aims to prevent large uncertainties in the interpolated data, possibly caused by missing raw data, from entering the wind vector reconstruction.

Linear extrapolation of $V_{\mathrm{r,interp}}(h)$ is permitted, as long as the vertical threshold requirement from the second filter is met. Finally, distortion effects on V_{r} due to translational platform motion are further taken into account by determining the LIDAR's current three-dimensional velocity vector $\mathbf{V}_{\mathrm{LIDAR,e}}$ in the Earth-fixed frame and subtracting its LOS directional component from the interpolated radial velocity:

$$V_{\mathrm{r,mod}}(h) = V_{\mathrm{r,interp}}(h) - \mathbf{V}_{\mathrm{LIDAR,e}} \cdot \mathbf{n}_{\mathrm{LOS,e}} \tag{17}$$

The modified values $V_{\mathrm{r,mod}}(h)$ are now used for the vector $\mathbf{b}(h)$ in Eq. 13, and the overdetermined LES (Eq. 9) is solved for each nominal height h using a least-squares algorithm. Each solution represents a motion-compensated wind vector $\mathbf{V}_{\mathrm{wind}}(h)$. The solving of the LES is only permitted when all of the latest five $V_{\mathrm{r,mod}}(h)$ are considered valid.

2.4 Motion data

The LIDAR's motion is measured using a high-frequency AHRS and a dedicated low-frequency dual-GPS receiver. Both instruments are installed on the uncrewed lightship close to the LIDAR; therefore, their measurements are assumed to represent the LIDAR's motion. The AHRS provides pitch and roll angles at an output frequency of $10\,\mathrm{Hz}$; however, its yaw and three-dimensional velocity measurements were excluded due to quality limitations. Instead, heading measurements from the dedicated dual-GPS receiver are used to determine the yaw angle ψ, while the velocity vector $\mathbf{V}_{\mathrm{LIDAR,e}}$ is derived from GPS data. As the dedicated dual GPS only provides horizontal position information, both the vertical component of $\mathbf{V}_{\mathrm{LIDAR,e}}$ and the vertical LIDAR offset Δz are extracted from the GPS files provided by the AHRS. The LIDAR's nominal position for $\Delta z = 0$ is mean sea level (MSL). Although the AHRS and the LIDAR are installed at a platform height of $5.5\,\mathrm{m}$ from the sea surface, the median Δz during November 2021 was measured to be $+0.53\,\mathrm{m}$, indicating an average LIDAR position slightly below MSL. All GPS information, including the dedicated dual GPS and the AHRS-internal GPS, is provided with an output frequency of $1\,\mathrm{Hz}$. An overview of the different parameters and their respective measuring instruments is shown in Table 1. Figure 6 displays the distributions of the ship's Euler angles during the investigated period as probability density functions (PDFs). In order to ensure the consistency of the motion data, a brief quality control procedure was performed. A timestamp check revealed several short periods where Universal-Time-Coordinated (UTC) timestamps were shifted by a magnitude of a few seconds. However, owing to a second source of individual data timestamps provided by a dedicated system clock, the UTC-indication errors were easily traceable and subsequently corrected. Furthermore, range checks and step checks were performed for each dataset. The respective thresholds used for each parameter are listed in Table A1 in the appendix. No violations of the range thresholds and only a few single violations of the step thresholds were observed. While visually reviewing every suspicious case, no significant anomalies were detected during the investigated period.

https://doi.org/10.5194/egusphere-2026-6846
Preprint. Discussion started: 12 November 2026
© Author(s) 2026. CC BY 4.0 License.

Table 1. Instruments and parameters used for the motion-compensation post-processing algorithm.

Instrument	Component	Parameter	Output frequency
Leosphere WindCube v2® pulsed wind lidar	–	LOS position	≈ 1 Hz
		$V_{\mathrm{r}}(h)$	
		$\mathrm{CNR}(h)$	
Magellan Professional 3011® dual GPS receiver	–	Yaw angle	1 Hz
		Horizontal position	
		Horizontal velocity	
Microstrain 3DM-GX3-35® AHRS	IMU	Pitch angle	10 Hz
		Roll angle	
	GPS receiver	Vertical position	1 Hz
		Vertical velocity	

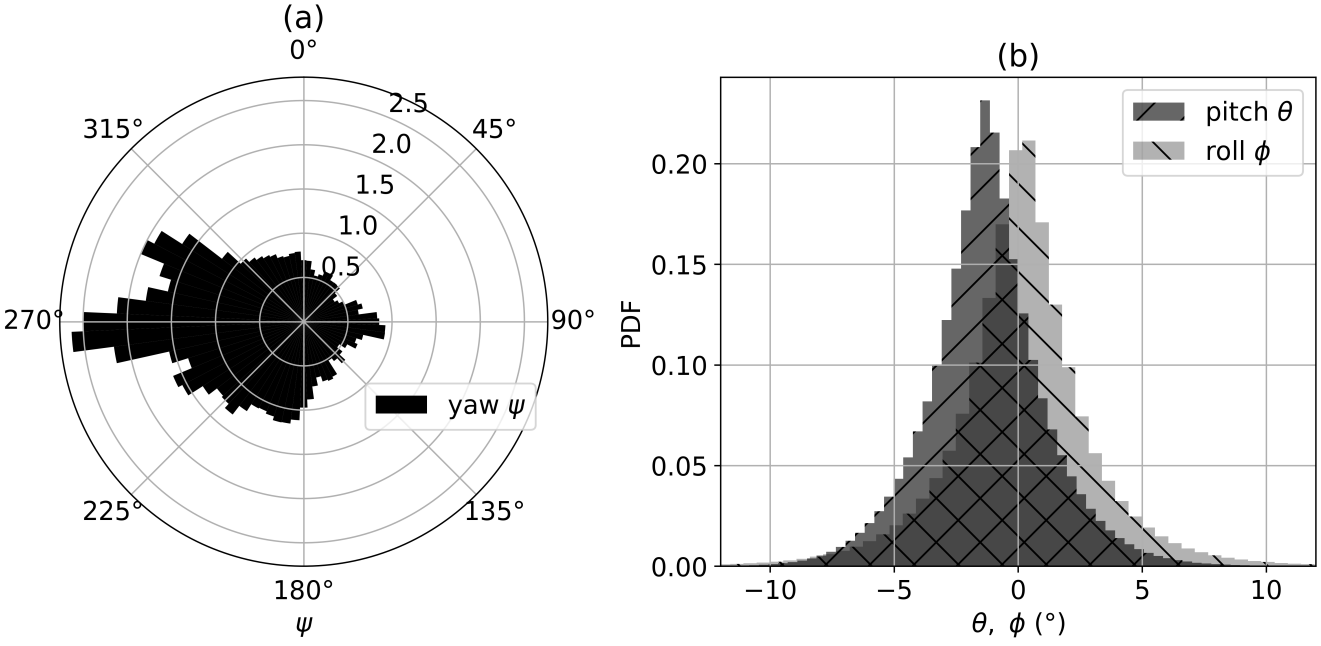


Figure 6. Distributions of the measured orientation angles of the uncrewed lightship UFS4 during November 2021. (a): Polar histogram of the dual-GPS-derived heading (yaw ψ), measured clockwise from geographical North. (b): Probability density distributions of AHRS-derived pitch θ and roll ϕ.

https://doi.org/10.5194/egusphere-2026-6846
Preprint. Discussion started: 12 November 2026
© Author(s) 2026. CC BY 4.0 License.

2.5 Data synchronization

Accurate temporal synchronization of the motion measurements and the high-frequency LIDAR data is essential for the correction algorithm. Because wave-induced ship motion is oscillatory, synchronization errors may increase rather than reduce motion-induced distortions by applying a correction corresponding to an incorrect platform state. For each LOS measurement, the required motion variables are interpolated from the corresponding sensor time series. Each LOS measurement is assigned a representative time t_{LOS}, defined as the midpoint between the start and end of the signal-accumulation interval. With the installed setup, the LIDAR is not internally synchronized with the motion sensors, allowing for a discrepancy $\Delta t_{\mathrm{LIDAR}}$ in timestamp indications. Instead, the AHRS and dual GPS datasets both contain UTC timestamps that are independently determined from received GPS time information. Both devices are additionally synchronized with a shared system clock, allowing for retrospective verification of their UTC timestamp alignment. However, the LIDAR uses an independent clock for its data timestamps. Although its time scale should theoretically comply with UTC as well, there is no option for verifying the accuracy of the LIDAR timestamps, especially regarding the effects of internal clock drift. Hence, an optimization-based synchronization method is proposed.

The method estimates the time shift $\Delta t_{\mathrm{LIDAR}}$ to be added to the LIDAR timestamps to align them with the motion measurements. It uses the residuals obtained from the least-squares solution of Eq. 9. For each reconstructed wind vector, the residual vector is defined as

$$\mathbf{r}(h) = \mathbf{b}(h) - \mathbf{A} \cdot \mathbf{V}_{\mathrm{wind}}(h) \tag{18}$$

Its components quantify the differences between the modified radial velocities used for the least-squares fit and those predicted by the reconstructed wind vector. The sum of squared residuals (SSR) is defined as

$$SSR(h) = \sum_{i=1}^{5} r_i(h)^2, \tag{19}$$

where i indexes the five LOS measurements used in the reconstruction. Lower SSR values indicate better agreement between these measurements and the fitted wind vector.

The synchronization procedure assumes that temporal misalignment increases the SSR because the motion correction applied to each LOS measurement no longer corresponds to the actual platform state at the time of acquisition. The SSR also reflects measurement noise as well as spatial and temporal variability of the wind field; it is therefore not a direct measure of synchronization accuracy. Figure 7 shows the dependence of the hourly mean SSR at the nominal height of $h = 97\,\mathrm{m}$, $\overline{SSR}_{97\,\mathrm{m}}$, on the applied time shift. For a one-hour sample window, this mean was calculated for a range of trial shifts $\Delta t_{\mathrm{LIDAR}}$ added to the LIDAR timestamps before motion compensation.

https://doi.org/10.5194/egusphere-2026-6846
Preprint. Discussion started: 12 November 2026
© Author(s) 2026. CC BY 4.0 License.

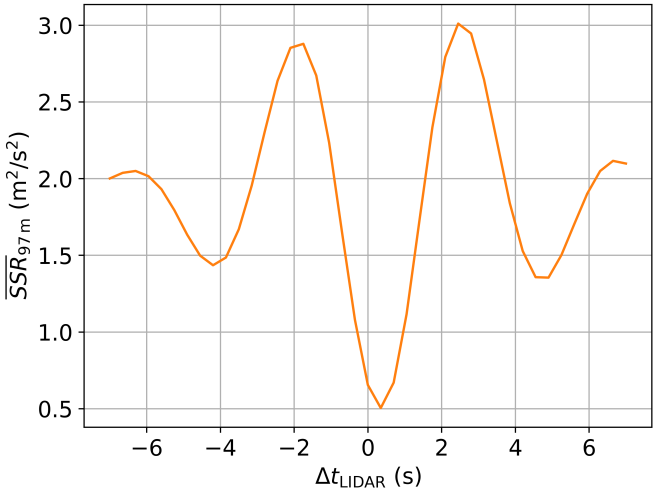


Figure 7. Hourly mean sum of squared residuals $\overline{SSR}$ at $h = 97\,\mathrm{m}$ as a function of the applied LIDAR timestamp shift $\Delta t_{\mathrm{LIDAR}}$ for the sample interval 00:00–01:00 on 1 November 2021. The minimum within the evaluated range occurs at approximately $\Delta t_{\mathrm{LIDAR}} = 0.35\,\mathrm{s}$.

The plot shows a smooth, oscillating pattern with several local minima, whose locations may relate to the dominating frequency of the platform's rotational motion. However, the global minimum is located at $\Delta t_{\mathrm{LIDAR}} \approx 0.35\,\mathrm{s}$, which is considered the estimated temporal alignment offset for this sample window. Similar patterns were observed for other time windows with sufficient data availability. Based on these findings, the hourly mean SSR at $h = 97\,\mathrm{m}$ is used as a target function $f(x)$ for an iterative optimization procedure, with x being $\Delta t_{\mathrm{LIDAR}}$. The evaluated height of $h = 97\,\mathrm{m}$ was chosen because it provided the highest LIDAR data availability during the investigation period. As each evaluation of the target function involves a time-consuming application of the post-processing procedure to the high-frequency LIDAR data, $f(x)$ should be minimized with the least amount of iterations possible in order to find the fitting $\Delta t_{\mathrm{LIDAR}}$.

Assuming that the minimum within the evaluated range is always the nearest one to $x = 0$, it is first bracketed by three sample points. This is achieved by successively shifting the start points $x_{1,2,3} = -1\,\mathrm{s}, 0\,\mathrm{s}, 1\,\mathrm{s}$ toward the negative gradient until $f(x_2) < f(x_1), f(x_3)$. From here, each iteration involves a parabolic fit through the three sample points and a calculation of the vertex as a minimum prediction. The target function is then evaluated at the vertex, replacing the current worst point (i.e. highest $f(x)$ value). The procedure is repeated until the new minimum prediction deviates no further than $0.01\,\mathrm{s}$ from the latest prediction.

The entire dataset was split into one-hour windows, and the described synchronization procedure was applied independently to each window to examine temporal variations in the alignment offset, including possible LIDAR clock drift. The resulting time series of estimated $\Delta t_{\mathrm{LIDAR}}$ is shown in Fig. 8.

https://doi.org/10.5194/egusphere-2026-6846
Preprint. Discussion started: 12 November 2026
© Author(s) 2026. CC BY 4.0 License.

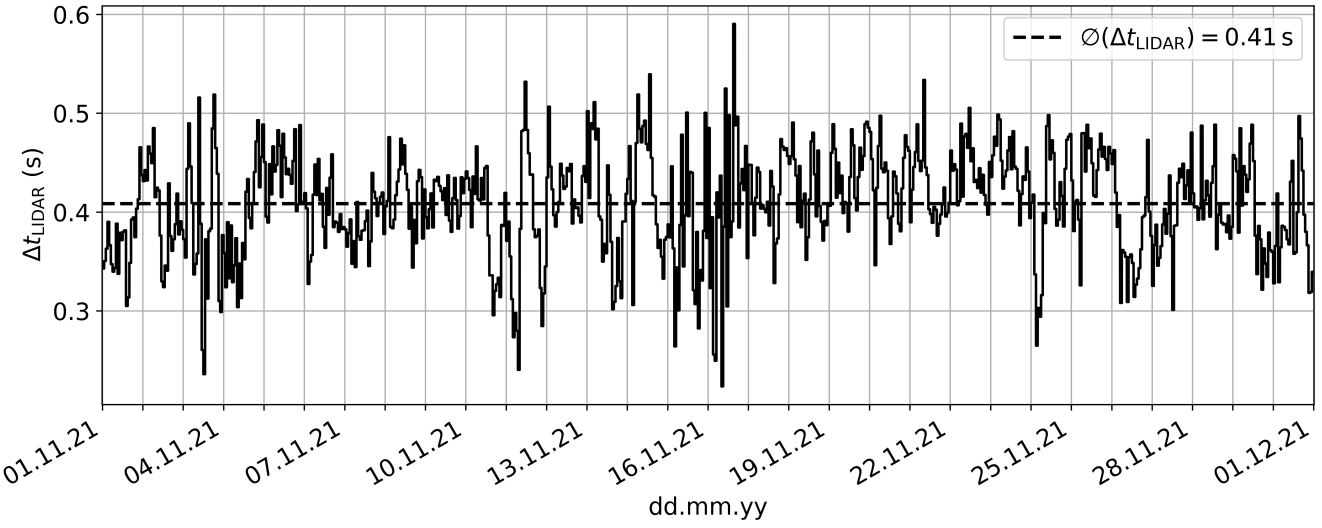


Figure 8. Time series of the estimated LIDAR timestamp shift $\Delta t_{\mathrm{LIDAR}}$, obtained by independently minimizing the hourly mean SSR at $h = 97\,\mathrm{m}$ for each one-hour window during November 2021. Positive values indicate shifts added to the original LIDAR timestamps.

Over the entire investigation period, the optimal time shift ranged from $+0.224\,\mathrm{s}$ to $+0.590\,\mathrm{s}$, with a mean value of $\Delta t_{\mathrm{LIDAR}} = +0.41\,\mathrm{s}$. Considering that this span is rather small and the plot does not show any clear indications of clock drift, the mean $\Delta t_{\mathrm{LIDAR}}$ was simply taken as a constant value and was applied to the entire LIDAR high-frequency dataset. The results obtained with the post-processing algorithm are presented in the following section.

3 Results

The combined effects of motion compensation, height interpolation, and changes in wind-vector reconstruction and filtering are assessed by comparing post-processed wind estimates with the original WindCube estimates without motion compensation, both at the high-frequency update scale (approximately 1 Hz) and at the 10-minute averaging scale.

As a plausibility check, wind-speed and wind-direction data are first compared to reference data available from the onboard DWD automatic weather station. Because these measurements were obtained at a different height, they do not constitute an independent validation of the corrected LIDAR measurements.

3.1 Availability of horizontal wind data

First, the availability of high-frequency horizontal wind data before and after post-processing is compared. At each nominal height h, availability is calculated independently for the uncorrected and post-processed data as the number of valid horizontal wind-speed estimates $N_{V,\,\mathrm{valid}}$ recorded during November 2021, divided by the potential total number of estimates $N_{V,\,\mathrm{total}}$:

$$DA = \frac{N_{V,\,\mathrm{valid}}}{N_{V,\,\mathrm{total}}} \tag{20}$$

https://doi.org/10.5194/egusphere-2026-6846
Preprint. Discussion started: 12 November 2026
© Author(s) 2026. CC BY 4.0 License.

Note that the total number of possible estimates $N_{V,\,\mathrm{total}}$ is higher for the post-processed data because of the change in the wind vector reconstruction method. Naturally, the least-squares solution can provide new horizontal wind data with each LOS measurement. In contrast, the original WindCube processing does not incorporate the vertical LOS for the horizontal components (see Eq. 4 and 5), leading to horizontal wind-speed estimates generally not being provided after vertical measurements.

Data Availability is generally limited by a filtering procedure involving the carrier-to-noise ratio (CNR). Raw radial velocities $V_\mathrm{r}(h)$ are rejected when the measured CNR is below $-23\,\mathrm{dB}$, leading to missing horizontal wind-speed estimates within the consecutive updates that require the respective $V_\mathrm{r}(h)$ value. This filter is implemented in both the uncorrected and the post-processed data. However, during post-processing, the interpolation of radial velocities to the predefined nominal heights also interferes with data availability, as radial velocities may be interpolated to nominal heights where the corresponding original V_r values are unavailable. As pointed out in Sect. 2.3, this effect is limited by the implemented interpolation requirement: The algorithm requires at least one valid raw $V_\mathrm{r}(h_\mathrm{true})$ measurement within the range $h \pm 10\,\mathrm{m}$ in order to accept the interpolated value $V_{\mathrm{r,\,interp}}(h)$. Notably, this requirement can also reduce availability in cases where an initially available V_r measurement is assigned to a true height h_true that is shifted by more than $10\,\mathrm{m}$ from the nominal height h, without a neighboring measurement replacing it in the allowed range.

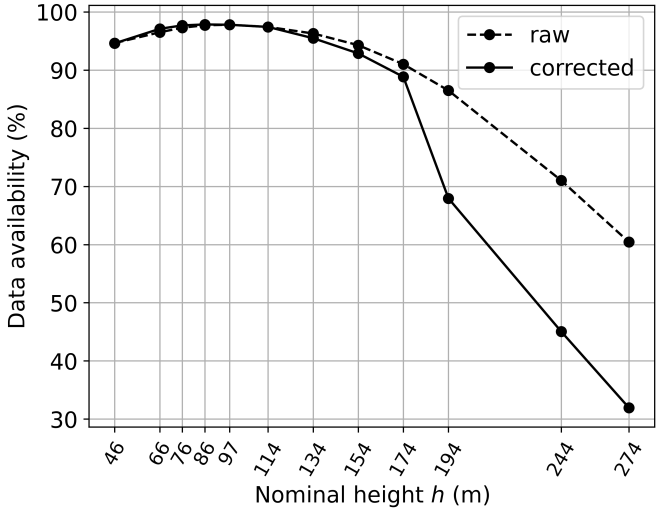


Figure 9. Availability of uncorrected (raw) and post-processed (corrected) LIDAR horizontal wind-speed estimates at the 12 predefined nominal measurement heights during November 2021.

Figure 9 shows approximately similar availability after post-processing up to $h = 174\,\mathrm{m}$, but substantially lower availability at the three highest nominal heights. These differences reflect the combined effects of CNR filtering and the height-interpolation requirement. At higher levels, wider spacing between measurement gates can increase the likelihood that no valid radial velocity measurement lies within $10\,\mathrm{m}$ of the target height. Future versions of the post-processing algorithm could incorporate different strategies for interpolating radial velocities in order to maintain higher data availability.

https://doi.org/10.5194/egusphere-2026-6846
Preprint. Discussion started: 12 November 2026
© Author(s) 2026. CC BY 4.0 License.

3.2 Plausibility assessment

The motion-compensated LIDAR measurements are compared with wind data from the DWD weather station's cup anemometer and wind vane, mounted aboard the lightship at approximately $14\,\mathrm{m}$ above the sea surface. The lowest nominal LIDAR measurement height is $46\,\mathrm{m}$. The DWD wind measurements are not corrected for ship motion. Together with the difference in measurement height, this limits the comparison to a qualitative plausibility assessment rather than a direct validation of the motion-compensated LIDAR data. The comparison uses one-minute mean wind speeds and wind directions to match the temporal resolution of the available DWD data. Intervals with LIDAR data availability below $50\,\%$ are excluded to reduce the influence of incomplete sampling. For the wind-direction comparison, intervals with a one-minute mean reference wind speed of $\overline{V}_{1\,\mathrm{min,ref}} < 5\,\mathrm{m\,s^{-1}}$ are additionally excluded. Figure 10 shows the time series of one-minute mean wind speeds and wind directions from the post-processed LIDAR at $h = 46\,\mathrm{m}$ and the DWD weather station.

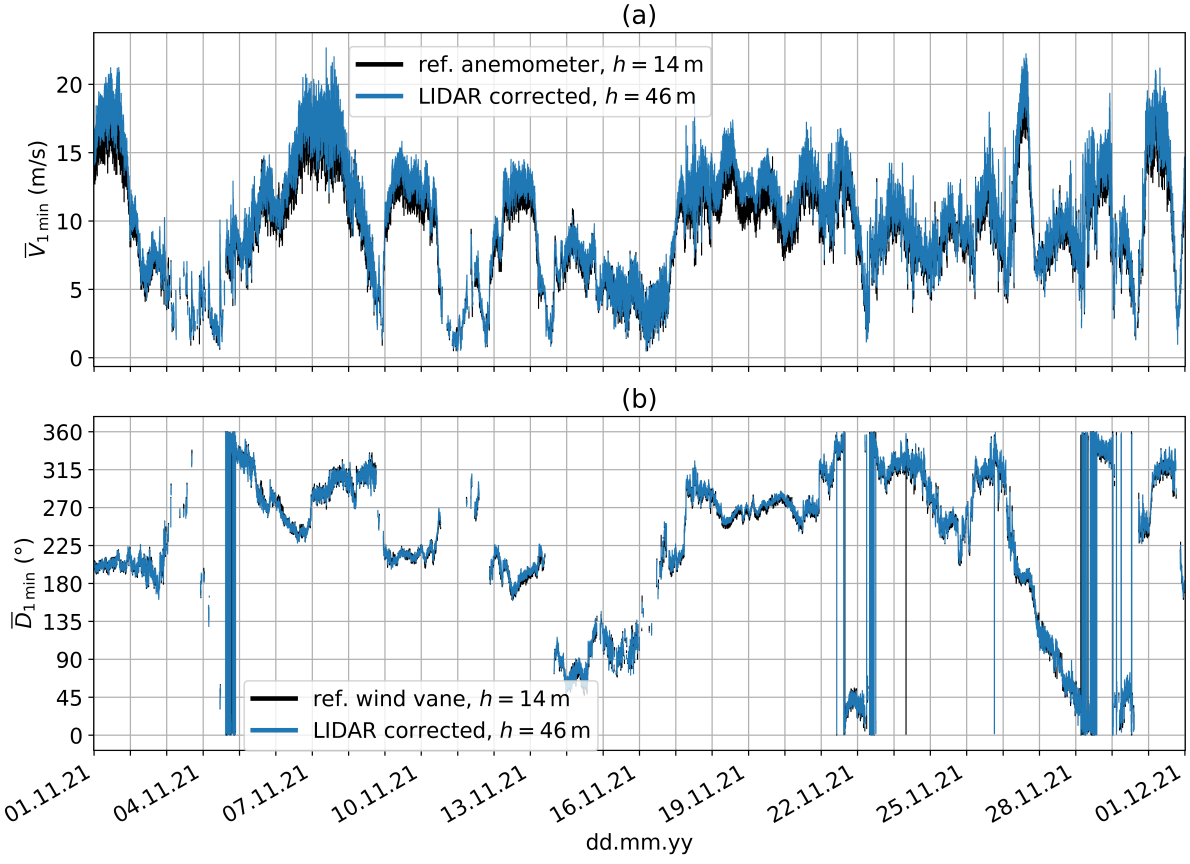


Figure 10. Comparison of one-minute mean wind speed $\overline{V}_{1\,\mathrm{min}}$ and wind direction $\overline{D}_{1\,\mathrm{min}}$ from the post-processed LIDAR at a nominal height of $h = 46\,\mathrm{m}$ and the DWD weather station's cup anemometer and wind vane at approximately $h = 14\,\mathrm{m}$ above the sea surface during November 2021. (a): Time series of $\overline{V}_{1\,\mathrm{min}}$, including only intervals with LIDAR data availability of at least $50\,\%$. (b): Time series of $\overline{D}_{1\,\mathrm{min}}$, including only intervals with LIDAR data availability of at least $50\,\%$ and $\overline{V}_{1\,\mathrm{min,ref}} \geq 5\,\mathrm{m\,s^{-1}}$.

https://doi.org/10.5194/egusphere-2026-6846
Preprint. Discussion started: 12 November 2026
© Author(s) 2026. CC BY 4.0 License.

The two datasets show similar temporal variations in wind speed and generally consistent wind directions. This qualitative agreement supports the plausibility of the post-processed LIDAR measurements at the lowest nominal height. Similar agreement was found for the remaining LIDAR nominal heights, although their time series are not shown here. Instead, the differences $\Delta\overline{V}_{1\,\mathrm{min}}$ and $\Delta\overline{D}_{1\,\mathrm{min}}$ of LIDAR wind-speed and wind-direction measurements from the corresponding reference data were calculated for several different LIDAR nominal heights to briefly examine the obtained vertical wind profiles. Differences in wind direction are calculated as circular differences according to

$$\Delta D = [(D_2 - D_1 + 180^\circ) \bmod 360^\circ] - 180^\circ, \tag{21}$$

which maps the differences to $[-180^\circ, 180^\circ)$. Here, $D_2 = \overline{D}_{1\,\mathrm{min,\,LIDAR}}$ and $D_1 = \overline{D}_{1\,\mathrm{min,\,ref}}$. Within the planetary boundary layer, the wind speed is generally expected to increase, and the wind direction is expected to turn clockwise with height, an effect known as the Ekman spiral (Businger, 1985). Both effects are represented by the distributions in Fig. 11, where positive mean differences of LIDAR measurements from the lower-height DWD measurements are observed in both one-minute wind-speed and wind-direction estimates, further supporting the plausibility of the corrected LIDAR measurements.

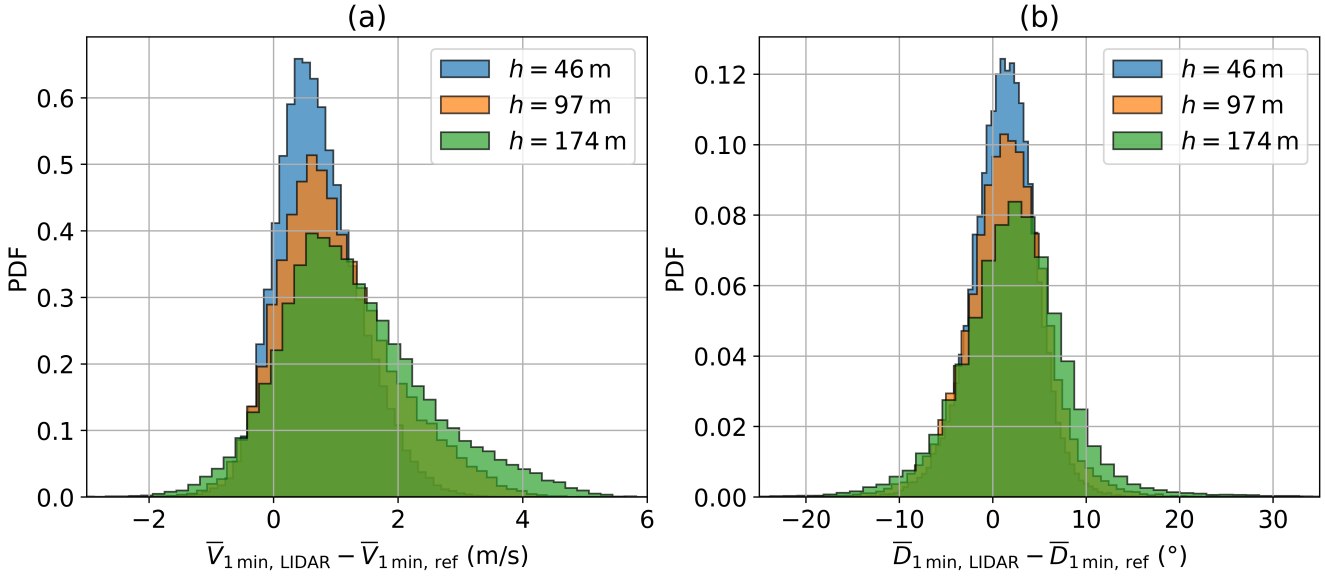


Figure 11. Differences in one-minute mean wind speeds $\overline{V}_{1\,\mathrm{min}}$ and wind directions $\overline{D}_{1\,\mathrm{min}}$ between the post-processed LIDAR at the indicated nominal heights and the DWD weather station at $h = 14\,\mathrm{m}$ during November 2021, displayed as probability density functions (PDFs). (a): Differences $\overline{V}_{1\,\mathrm{min,\,LIDAR}} - \overline{V}_{1\,\mathrm{min,\,ref}}$, including only intervals with LIDAR data availability of at least 50 %. (b): Circular differences $[(\overline{D}_{1\,\mathrm{min,\,LIDAR}} - \overline{D}_{1\,\mathrm{min,\,ref}} + 180^\circ) \bmod 360^\circ] - 180^\circ$, including only intervals with LIDAR data availability of at least 50 % and $\overline{V}_{1\,\mathrm{min,\,ref}} \geq 5\,\mathrm{m\,s^{-1}}$.

https://doi.org/10.5194/egusphere-2026-6846
Preprint. Discussion started: 12 November 2026
© Author(s) 2026. CC BY 4.0 License.

3.3 Effects of motion compensation on horizontal wind speed

We now examine how motion compensation affects reconstructed horizontal wind speed by comparing the uncorrected LIDAR data with the post-processed data at different temporal resolutions. The analysis is first carried on the level of high-frequency reconstructed wind vectors (approximately 1 Hz), followed by 10-minute mean values calculated from these high-frequency data.

3.3.1 High-Frequency wind-speed data

Figures 12 and 13 compare uncorrected and motion-compensated high-frequency horizontal wind speeds at the nominal measurement height of $h = 97\,\mathrm{m}$. An overview is provided by Fig. 12, where the post-processed values are plotted against the corresponding uncorrected values from the same individual time steps, as a scatter plot and as a probability-density heat map. Additionally, Fig. 13 shows the corresponding high-frequency time series (a) and the differences $\Delta V = V_{\mathrm{cor}} - V_{\mathrm{raw}}$ for individual data pairs (b). Summary statistics of these differences at nominal heights of $46\,\mathrm{m}$, $97\,\mathrm{m}$, and $174\,\mathrm{m}$ are reported in Table 2.

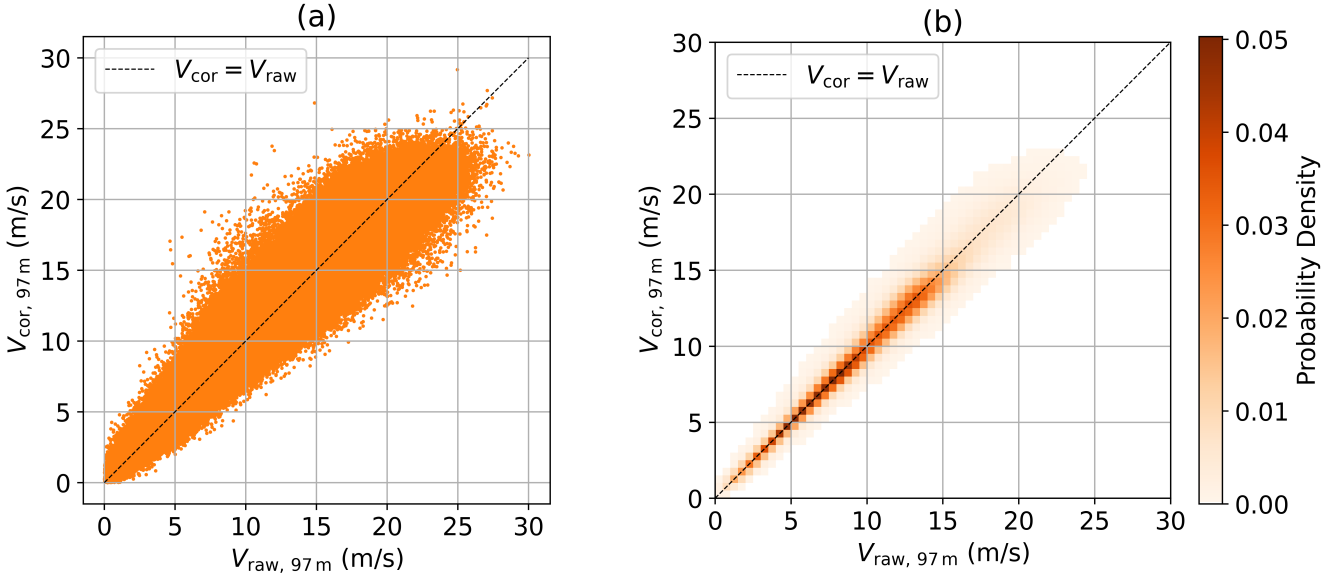


Figure 12. Comparison of the motion-compensated horizontal wind speed V_{cor} and the uncorrected wind speed V_{raw} at the nominal LIDAR measurement height of $h = 97\,\mathrm{m}$ during November 2021: (a) Scatter plot: Each point represents a pair of high-frequency estimates associated with the same original LIDAR timestamp. (b) Probability-density heat map.

https://doi.org/10.5194/egusphere-2026-6846
Preprint. Discussion started: 12 November 2026
© Author(s) 2026. CC BY 4.0 License.

Table 2. Summary statistics of high-frequency horizontal wind-speed differences $\Delta V = V_{\mathrm{cor}} - V_{\mathrm{raw}}$ at the indicated nominal LIDAR measurement heights during November 2021. Difference statistics are reported in m s^{-1}; the final column gives the availability of valid corrected–uncorrected data pairs.

Measurement height	Mean	Std. dev.	Min.	Max.	Data pair availability
46 m	−0.027	0.963	−9.164	+12.780	94.6 %
97 m	−0.033	0.975	−10.173	+12.432	97.7 %
174 m	−0.045	0.998	−10.254	+13.318	88.8 %

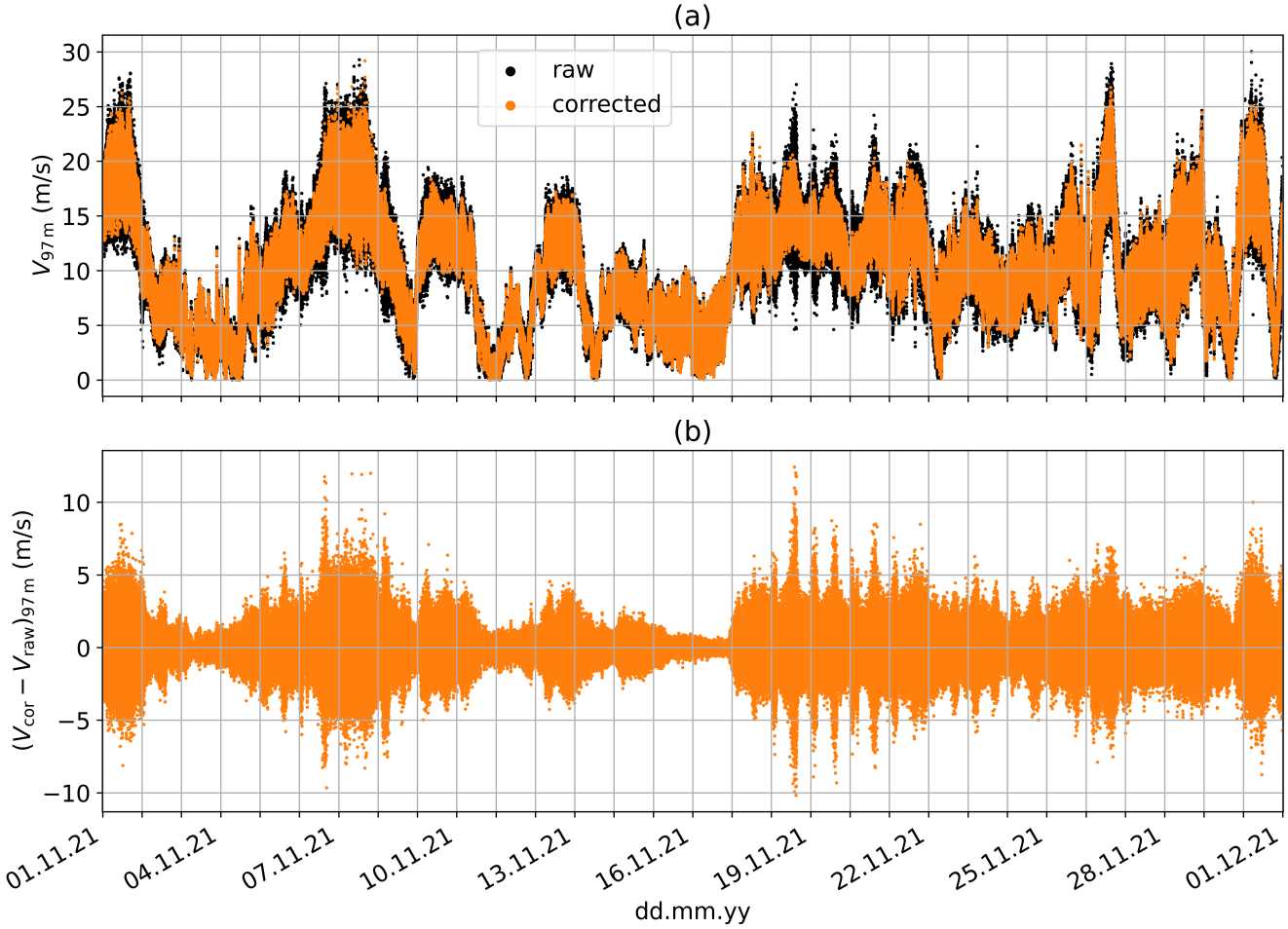


Figure 13. (a) Time series of uncorrected (V_{raw}) and motion-compensated (V_{cor}) LIDAR horizontal wind speed at the nominal measurement height of $h = 97\,\mathrm{m}$ during November 2021, shown at the high-frequency wind-vector update rate (approximately 1 Hz). (b) Differences $\Delta V = V_{\mathrm{cor}} - V_{\mathrm{raw}}$ for individual data pairs.

https://doi.org/10.5194/egusphere-2026-6846
Preprint. Discussion started: 12 November 2026
© Author(s) 2026. CC BY 4.0 License.

Figure 13(a) shows reduced short-term variability in the corrected data, particularly during periods of higher wind speed. This is consistent with the suppression of motion-induced fluctuations. The associated changes in wind-speed variability and LIDAR-derived turbulence intensity are further examined in Section 3.4. The difference time series in Fig. 13(b) also reveals larger changes to individual estimates during periods of higher wind speed, with differences exceeding $5\,\mathrm{m\,s^{-1}}$ in magnitude. The scatter plot in Fig. 12(a) indicates that post-processing tends to slightly reduce V estimates at the upper limit of the observed wind-speed range. However, the heat map representation in Fig. 12(b) reveals that a large portion of the data is only affected by a small degree. Despite substantial changes to some individual estimates, the overall mean differences remain small, ranging from $-0.027\,\mathrm{m\,s^{-1}}$ to $-0.045\,\mathrm{m\,s^{-1}}$ across the three heights (Table 2). The standard deviation of the differences increases only slightly with height, from $0.963\,\mathrm{m\,s^{-1}}$ at $46\,\mathrm{m}$ to $0.998\,\mathrm{m\,s^{-1}}$ at $174\,\mathrm{m}$. This increase seems to reflect mostly the higher baseline wind speeds at greater heights. The dominant effect is therefore a change in short-term variability rather than a substantial shift in the overall mean wind speed.

To examine how the distributions of ΔV vary between wind-speed conditions, the high-frequency data are grouped according to the uncorrected wind speed at the respective nominal height h. The following classification is applied to the data at all investigated heights:

- Weak wind: $V_{\mathrm{raw}}(h) < 6\,\mathrm{m\,s^{-1}}$
- Moderate wind: $6\,\mathrm{m\,s^{-1}} \leq V_{\mathrm{raw}}(h) < 12\,\mathrm{m\,s^{-1}}$
- Strong wind: $V_{\mathrm{raw}}(h) \geq 12\,\mathrm{m\,s^{-1}}$

Figure 14 shows the resulting distributions at $h = 97\,\mathrm{m}$, while Table 3 reports the corresponding statistics for all three heights. Note that the wind-speed categories are defined independently for each height, using the respective uncorrected $V_{\mathrm{raw}}(h)$ measurements. Motion-induced fluctuations in these measurements may therefore influence which category a measurement belongs to. The reported mean differences show how much post-processing changes the wind-speed estimates within each category; they do not quantify measurement errors relative to the true wind speed.

The distributions broaden from the weak-wind to the strong-wind category (Fig. 14). At $h = 97\,\mathrm{m}$, the standard deviation of ΔV increases from $0.498\,\mathrm{m\,s^{-1}}$ for weak wind to $0.859\,\mathrm{m\,s^{-1}}$ for moderate wind and $1.237\,\mathrm{m\,s^{-1}}$ for strong wind. Similar changes are observed at $h = 46\,\mathrm{m}$ and $h = 174\,\mathrm{m}$ (Table 3), confirming the overall increasing influence of post-processing with higher measured wind speeds. This behavior is expected, as the measurements are likely to be more affected by stronger wind- and wave-induced platform motion. The weak-wind and moderate-wind categories have small positive conditional mean differences at all three heights, whereas the strong-wind category has negative conditional mean differences. These shifts are partly caused by the bias that is introduced due to the classification based on the uncorrected wind speed. At $h = 46\,\mathrm{m}$, raw V measurements above $12\,\mathrm{m\,s^{-1}}$ are corrected by $-0.258\,\mathrm{m\,s^{-1}}$, on average. Individual differences can be much larger than these conditional means, reaching approximately $+13.3\,\mathrm{m\,s^{-1}}$ and $-10.3\,\mathrm{m\,s^{-1}}$ across the investigated heights. These results describe how motion compensation changes the estimates within the selected raw-wind-speed categories; they do not establish which estimates are closer to the true wind speed.

https://doi.org/10.5194/egusphere-2026-6846
Preprint. Discussion started: 12 November 2026
© Author(s) 2026. CC BY 4.0 License.

Table 3. Summary statistics of the differences $\Delta V = V_{\mathrm{cor}} - V_{\mathrm{raw}}$ between motion-compensated and uncorrected high-frequency horizontal wind speeds at the indicated nominal LIDAR measurement heights during November 2021, grouped by uncorrected wind speed category. Difference statistics are reported in $\mathrm{m\,s^{-1}}$; the final column gives each category's share of valid data pairs at the corresponding height.

Category	Measurement height	Mean	Std. dev.	Min.	Max.	Share of valid data pairs (%)
Weak wind	46 m	+0.077	0.511	−3.050	+12.685	18.5
	97 m	+0.066	0.498	−3.093	+12.432	18.9
	174 m	+0.067	0.493	−3.205	+11.258	16.1
Moderate wind	46 m	+0.108	0.844	−5.463	+12.780	46.2
	97 m	+0.106	0.859	−5.203	+12.027	44.3
	174 m	+0.108	0.868	−5.363	+13.318	44.3
Strong wind	46 m	−0.258	1.214	−9.164	+11.619	35.4
	97 m	−0.231	1.237	−10.173	+11.956	36.8
	174 m	−0.232	1.240	−10.254	+10.996	39.6

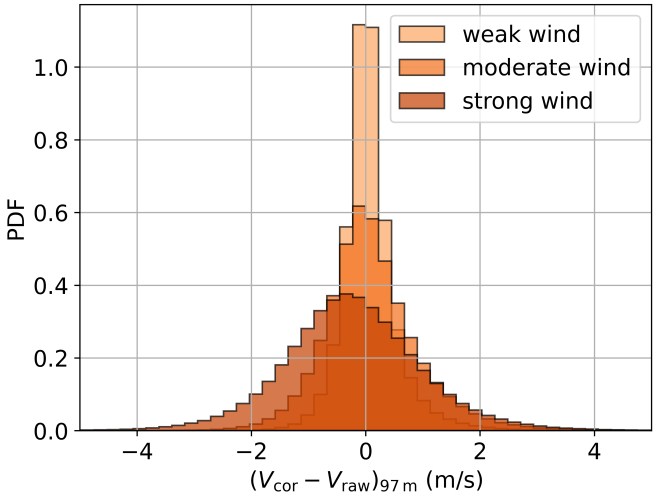


Figure 14. Probability densities of the differences $\Delta V = V_{\mathrm{cor}} - V_{\mathrm{raw}}$ between motion-compensated and uncorrected high-frequency horizontal wind-speeds at the nominal LIDAR measurement height of $h = 97\,\mathrm{m}$ during November 2021, grouped by uncorrected wind-speed categories. The displayed range is limited to $\pm 5\,\mathrm{m\,s^{-1}}$; minimum and maximum values for the full distributions are reported in Table 3.

https://doi.org/10.5194/egusphere-2026-6846
Preprint. Discussion started: 12 November 2026
© Author(s) 2026. CC BY 4.0 License.

3.3.2 10-Minute statistical data

The comparison is repeated using 10-minute mean horizontal wind speeds $\overline{V}$ that are retrieved from the high-frequency esti-
370 mates through scalar averaging. Figure 15 shows the motion-compensated values plotted against the corresponding uncorrected values at the nominal LIDAR measurement height of $h = 97\,\mathrm{m}$. Figure 16 shows the corresponding time series (a) and the differences $\Delta\overline{V} = \overline{V}_{\mathrm{cor}} - \overline{V}_{\mathrm{raw}}$ for each interval (b). Summary statistics of these differences at all three investigated heights are reported in Table 4. Intervals with raw or corrected data availability below $50\,\%$ are excluded to reduce the influence of incomplete sampling.

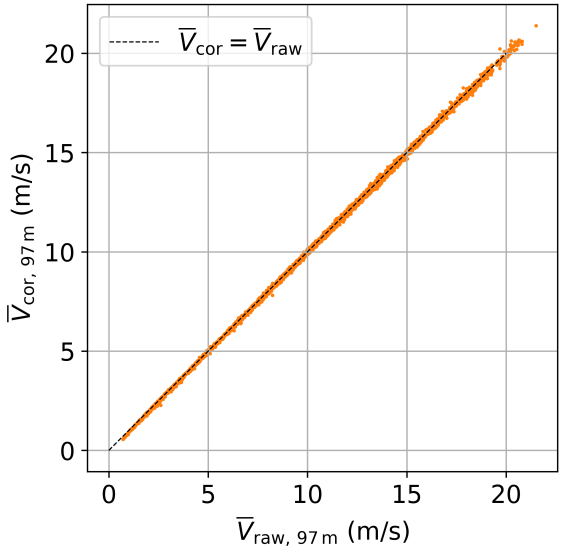


Figure 15. Comparison of the motion-compensated 10-minute mean horizontal wind speed $\overline{V}_{\mathrm{cor}}$ and the uncorrected equivalent $\overline{V}_{\mathrm{raw}}$ at the nominal LIDAR measurement height of $h = 97\,\mathrm{m}$ during November 2021 as a scatter plot. Each point represents an individual data pair sharing the same time interval. Only intervals with raw and corrected data availability of at least $50\,\%$ are included.

375 The application of post-processing has only a small effect on 10-minute mean wind-speed estimates. Across the three heights, the mean differences range from $-0.037\,\mathrm{m\,s^{-1}}$ to $-0.028\,\mathrm{m\,s^{-1}}$, indicating a small average decrease after correction (Table 4). This corresponds approximately to the averages observed for the high-frequency data. The standard deviations of $\Delta\overline{V}$ range from $0.079\,\mathrm{m\,s^{-1}}$ to $0.086\,\mathrm{m\,s^{-1}}$, and the largest absolute difference in the retained dataset is $0.540\,\mathrm{m\,s^{-1}}$. As expected, individual differences $\Delta\overline{V}$ between the 10-minute means after scalar averaging are much less variable than the differences ΔV
380 between high-frequency estimates, whose standard deviations are close to $1\,\mathrm{m\,s^{-1}}$ (see Table 2).

https://doi.org/10.5194/egusphere-2026-6846
Preprint. Discussion started: 12 November 2026
© Author(s) 2026. CC BY 4.0 License.

Table 4. Summary statistics of the differences $\Delta\overline{V} = \overline{V}_{\mathrm{cor}} - \overline{V}_{\mathrm{raw}}$ between motion-compensated and uncorrected 10-minute mean horizontal wind speeds at the indicated nominal LIDAR measurement heights during November 2021. Only intervals with raw and corrected data availability of at least 50 % are included. Difference statistics are reported in m s^{-1}; N denotes the number of valid data pairs.

Measurement height	Mean	Std. dev.	Min.	Max.	N
46 m	−0.028	0.080	−0.479	+0.499	4104
97 m	−0.035	0.079	−0.441	+0.540	4256
174 m	−0.037	0.086	−0.479	+0.531	3954

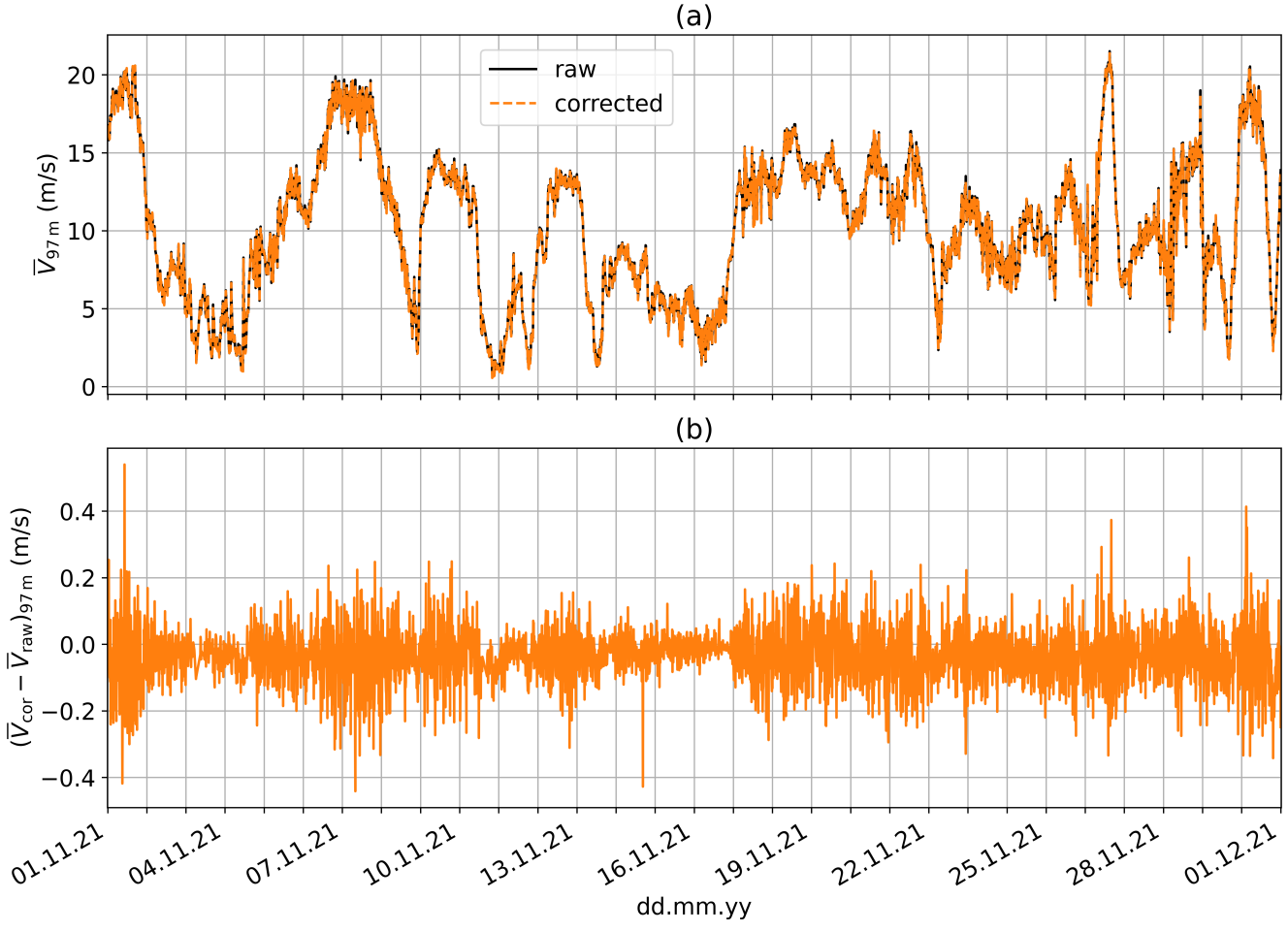


Figure 16. (a) Time series of uncorrected ($\overline{V}_{\mathrm{raw}}$) and motion-compensated ($\overline{V}_{\mathrm{cor}}$) LIDAR 10-minute mean horizontal wind speed at the nominal measurement height of $h = 97\,\mathrm{m}$ during November 2021. (b) Differences $\Delta\overline{V} = \overline{V}_{\mathrm{cor}} - \overline{V}_{\mathrm{raw}}$ between the corrected and uncorrected means. Only intervals with raw and corrected data availability of at least 50 % are included.

https://doi.org/10.5194/egusphere-2026-6846
Preprint. Discussion started: 12 November 2026
© Author(s) 2026. CC BY 4.0 License.

The 10-minute intervals are further grouped by wind-speed categories analogous to the high-frequency data, using the uncorrected 10-minute mean wind speed at the respective height h:

- Weak wind: $\overline{V}_{\mathrm{raw}}(h) < 6\,\mathrm{m\,s^{-1}}$
- Moderate wind: $6\,\mathrm{m\,s^{-1}} \leq \overline{V}_{\mathrm{raw}}(h) < 12\,\mathrm{m\,s^{-1}}$
- Strong wind: $\overline{V}_{\mathrm{raw}}(h) \geq 12\,\mathrm{m\,s^{-1}}$

Figure 17 shows the resulting distributions of $\Delta\overline{V}$ at $h = 97\,\mathrm{m}$, while Table 5 summarizes the statistics for all three heights. As stated before, the group averages describe how much post-processing changes the estimates for intervals selected using the raw wind speed. They do not quantify measurement errors relative to the true wind speed.

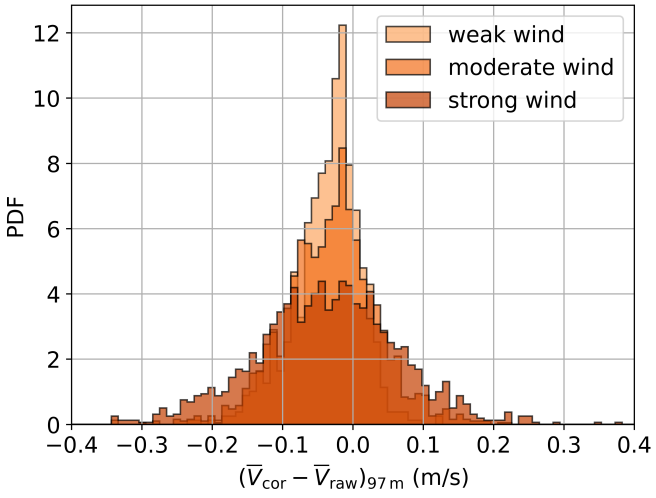


Figure 17. Probability densities of the differences $\Delta\overline{V} = \overline{V}_{\mathrm{cor}} - \overline{V}_{\mathrm{raw}}$ between motion-compensated and uncorrected 10-minute mean horizontal wind speeds at the nominal LIDAR measurement height of $h = 97\,\mathrm{m}$ during November 2021, grouped by uncorrected 10-minute mean wind speed. Only intervals with raw and corrected LIDAR data availability of at least $50\,\%$ are included.

All three wind-speed categories show small average decreases after post-processing, with mean differences ranging from $-0.042\,\mathrm{m\,s^{-1}}$ to $-0.026\,\mathrm{m\,s^{-1}}$ across the investigated heights. In the strong-wind category, the mean $\Delta\overline{V}$ becomes slightly more negative with height, reaching $-0.042\,\mathrm{m\,s^{-1}}$ at $h = 174\,\mathrm{m}$. Similar to the high-frequency data, the spread of the differences increases from the weak-wind to the strong-wind category, although the standard deviations of $\Delta\overline{V}$ remain small by comparison. At $h = 97\,\mathrm{m}$, the standard deviation increases from $0.049\,\mathrm{m\,s^{-1}}$ for weak wind to $0.067\,\mathrm{m\,s^{-1}}$ for moderate wind and $0.103\,\mathrm{m\,s^{-1}}$ for strong wind. Similar trends occur at the other two heights (Table 5).

In the unfiltered comparison, a few differences exceeded $1\,\mathrm{m\,s^{-1}}$ in magnitude. These occurred in intervals with LIDAR data availability below $50\,\%$ and are excluded from the results reported here. Their association with low availability suggests that incomplete temporal sampling may also influence differences between the 10-minute means. For intervals meeting the availability criterion, post-processing changes the 10-minute mean wind speed only slightly.

https://doi.org/10.5194/egusphere-2026-6846
Preprint. Discussion started: 12 November 2026
© Author(s) 2026. CC BY 4.0 License.

Table 5. Summary statistics of the differences $\Delta\overline{V} = \overline{V}_{\mathrm{cor}} - \overline{V}_{\mathrm{raw}}$ between motion-compensated and uncorrected 10-minute mean horizontal wind speeds at the indicated nominal LIDAR measurement heights during November 2021, grouped by uncorrected 10-minute mean wind speed. Only intervals with raw and corrected data availability of at least 50 % are included. Difference statistics are reported in $\mathrm{m\,s^{-1}}$; the final column gives each category's share of valid data pairs at the corresponding height.

Category	Measurement height	Mean	Std. dev.	Min.	Max.	Share of valid data pairs (%)
Weak wind	46 m	−0.034	0.049	−0.313	+0.120	17.8
	97 m	−0.036	0.049	−0.342	+0.127	18.4
	174 m	−0.038	0.053	−0.268	+0.120	15.6
Moderate wind	46 m	−0.026	0.066	−0.479	+0.263	45.7
	97 m	−0.032	0.067	−0.428	+0.222	44.4
	174 m	−0.032	0.070	−0.366	+0.275	43.7
Strong wind	46 m	−0.029	0.103	−0.395	+0.499	36.5
	97 m	−0.036	0.103	−0.441	+0.540	37.1
	174 m	−0.042	0.110	−0.479	+0.531	40.7

3.4 Effects of motion compensation on horizontal wind-speed variability

Section 3.3.1 showed reduced short-term variability in the post-processed wind-speed estimates. This change is quantified in the following, using the standard deviation of individual horizontal wind-speed estimates within each 10-minute interval, $\sigma_{10\,\mathrm{min}}(V)$. Normalizing this quantity by the corresponding 10-minute mean wind speed $\overline{V}$ gives the LIDAR-derived turbulence intensity:

$$TI = \frac{\sigma_{10\,\mathrm{min}}(V)}{\overline{V}}. \tag{22}$$

TI is calculated separately from the raw and post-processed data using the individual high-frequency and 10-min mean estimates from each interval. Temporal sampling resolution, spatial averaging, sequential beam sampling, and wind-vector reconstruction influence the variability represented by these estimates. The resulting TI is therefore treated here as an apparent LIDAR-derived quantity. Figure 18 compares the time series of $\sigma_{10\,\mathrm{min}}(V)$ and TI at the nominal measurement height of $h = 97\,\mathrm{m}$. Table 6 reports the arithmetic mean of the individual 10-minute TI values within different wind-speed categories as defined in the preceding subsection, using the uncorrected 10-minute mean wind speed $\overline{V}_{\mathrm{raw}}(h)$ for classification. Intervals with data availability below $50\,\%$ are excluded.

The time series show reductions in both the standard deviation of the wind-speed estimates and the apparent TI after post-processing (Fig. 18). Mean TI values are lower at all three heights and in all wind-speed categories (Table 6). The absolute reductions are approximately 0.04 in the weak-wind category and 0.03 in the moderate-wind and strong-wind categories. This is consistent with previous observations by Désert et al. (2021), where motion-induced LIDAR measurements were found to

https://doi.org/10.5194/egusphere-2026-6846
Preprint. Discussion started: 12 November 2026
© Author(s) 2026. CC BY 4.0 License.

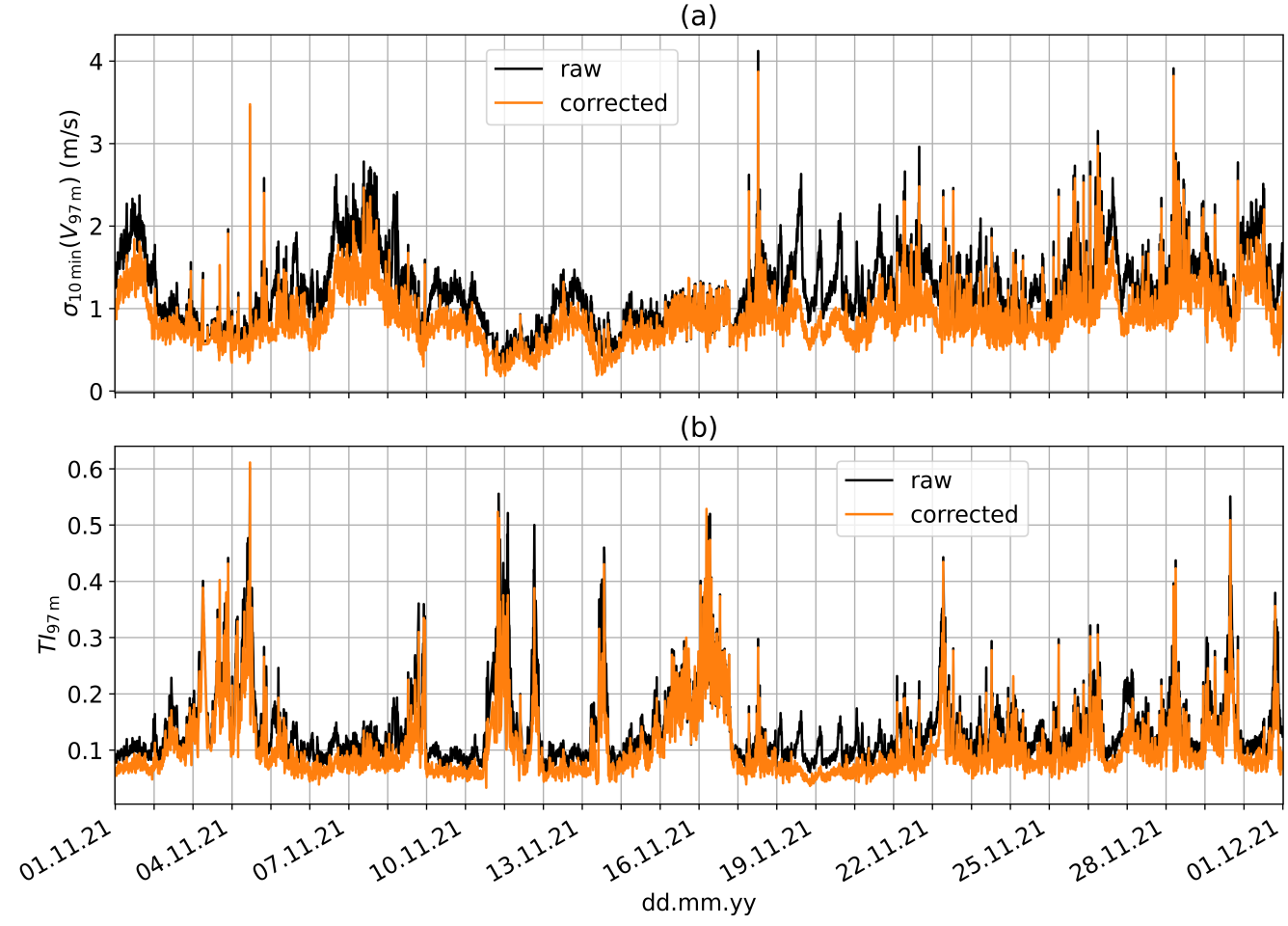


Figure 18. Time series of horizontal wind-speed variability at the nominal LIDAR measurement height of $h = 97\,\mathrm{m}$ during November 2021, comparing uncorrected (raw) and post-processed (corrected) data. (a) Standard deviation of the individual horizontal wind-speed estimates within each 10-minute interval, $\sigma_{10\,\mathrm{min}}(V)$. (b) Corresponding LIDAR-derived turbulence intensity, $TI = \sigma_{10\,\mathrm{min}}(V)/\overline{V}$. Only intervals with raw and corrected data availability of at least $50\,\%$ are included.

overestimate TI by approximately 0.03 compared to a fixed LIDAR. However, it remains unclear how much of this reduction is, in fact, related to the compensation for platform motion, considering that the post-processing algorithm uses a different technique for wind-vector reconstruction than the internal WindCube algorithm. Possibly, the involvement of the least-squares procedure for solving the overdetermined LES may itself affect the variability of the reconstructed wind field compared to the approach based on Eq. 4–6. An independent turbulence reference would additionally be required to assess the accuracy of the TI estimates.

https://doi.org/10.5194/egusphere-2026-6846
Preprint. Discussion started: 12 November 2026
© Author(s) 2026. CC BY 4.0 License.

Table 6. Arithmetic mean of the individual 10-minute LIDAR-derived TI values, $\langle TI \rangle$, at the indicated nominal measurement heights during November 2021. Wind-speed categories are defined in Section 3.3.2 using the uncorrected 10-minute mean wind speed $\overline{V}_{\mathrm{raw}}(h)$. Only intervals with raw and corrected data availability of at least 50 % are included. TI is dimensionless.

Measurement height	Data	Weak wind	Moderate wind	Strong wind
46 m	Raw	0.236	0.127	0.106
	Corrected	0.199	0.096	0.078
97 m	Raw	0.233	0.126	0.102
	Corrected	0.192	0.094	0.072
174 m	Raw	0.244	0.126	0.099
	Corrected	0.207	0.095	0.068

3.5 Effects of motion compensation on vertical wind speed

The vertical velocity component w is examined next. Its mean is generally expected to be close to $0\,\mathrm{m\,s^{-1}}$, although its variability depends on atmospheric conditions and possibly the influence of wakes created by nearby wind farms. To assess the effect of post-processing, Fig. 19 compares the distributions of uncorrected and post-processed high-frequency w estimates at $h = 97\,\mathrm{m}$, while Table 7 summarizes their statistics at selected measurement heights. The uncorrected values originate from the raw vertical LOS measurements and are therefore directly associated with the moving LIDAR reference frame, whereas the corrected values are extracted from the post-processed reconstructed wind vectors and refer to the Earth-fixed frame.

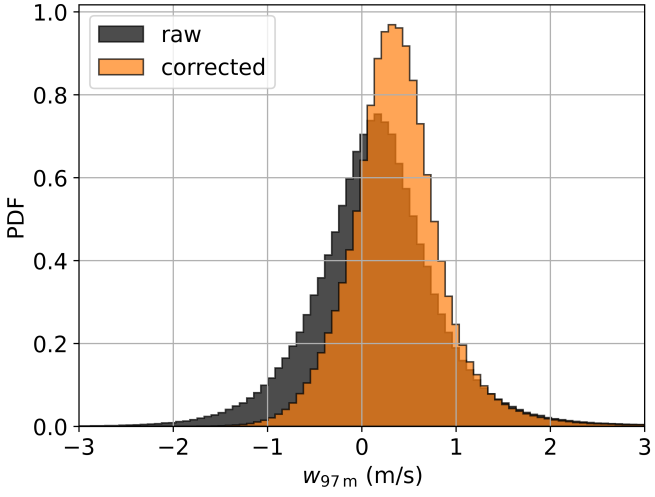


Figure 19. Probability density of high-frequency w estimates at $h = 97\,\mathrm{m}$ during November 2021, comparing uncorrected (raw) LIDAR data in the instrument frame with motion-compensated (corrected) data in the Earth-fixed frame. Positive w denotes downward vertical velocity within the respective reference frames. The displayed range is restricted to $\pm 3\,\mathrm{m\,s^{-1}}$; the full minima and maxima are reported in Table 7.

https://doi.org/10.5194/egusphere-2026-6846
Preprint. Discussion started: 12 November 2026
© Author(s) 2026. CC BY 4.0 License.

Table 7. Summary statistics of high-frequency w estimates at the indicated nominal LIDAR measurement heights during November 2021. Raw values are expressed in the instrument frame, and corrected values in the Earth-fixed frame. Positive w denotes downward vertical velocity within the respective reference frames. Velocity statistics are reported in $\mathrm{m\,s^{-1}}$; the final column gives the availability of high-frequency w estimates.

Measurement height	Data	Mean	Std. dev.	Min.	Max.	Data availability (%)
46 m	Raw	0.120	0.652	−5.404	18.702	95.4
	Corrected	0.348	0.484	−2.568	6.116	94.6
97 m	Raw	0.150	0.696	−6.183	8.854	98.2
	Corrected	0.380	0.529	−2.654	6.666	97.8
174 m	Raw	0.164	0.742	−6.026	9.215	92.4
	Corrected	0.408	0.557	−3.373	7.049	88.8

The corrected distributions have smaller standard deviations at all investigated heights, indicating reduced variability in the reported w estimates. At $h = 97\,\mathrm{m}$, the standard deviation decreases from $0.696\,\mathrm{m\,s^{-1}}$ to $0.529\,\mathrm{m\,s^{-1}}$. The minima and maxima are also less extreme after processing. However, the two sets of statistics are not necessarily based on identical samples, as indicated by the different data availabilities. Possibly, significant outliers were simply filtered due to the height interpolation requirement during post-processing. These distribution-level results therefore do not establish how individual extreme values change after correction.

Meanwhile, the average measured w increases from $0.120\,\mathrm{m\,s^{-1}}$ – $0.164\,\mathrm{m\,s^{-1}}$ in the raw data to $0.348\,\mathrm{m\,s^{-1}}$ – $0.408\,\mathrm{m\,s^{-1}}$ in the corrected data. Under the adopted sign convention, the positive mean values indicate a downward velocity component. A persistent platform tilt, e.g. due to unbalanced load distribution on the ship, could contribute to the positive raw means by projecting horizontal flow onto the instrument's nominal vertical axis. An unaccounted angular offset between the AHRS and LIDAR reference frames could similarly introduce a horizontal-flow contribution into the corrected vertical component. Neither explanation can be confirmed from the present comparison, and the positive corrected means alone do not establish a persistent atmospheric downward flow.

As discussed in Sect. 3.4, post-processing changes both the treatment of platform motion and the wind-vector reconstruction method. The observed reduction in variability therefore cannot be attributed solely to motion compensation. A comparison using the same reconstruction method and matching valid timestamps, with motion compensation enabled and disabled, would help distinguish these effects. Without independent vertical-velocity measurements at comparable heights, the accuracy of the corrected w estimates and the contributions of atmospheric variability and residual measurement or reconstruction errors remain unresolved.

https://doi.org/10.5194/egusphere-2026-6846
Preprint. Discussion started: 12 November 2026
© Author(s) 2026. CC BY 4.0 License.

3.6 Effects of motion compensation on wind direction

The wind direction D reported by the LIDAR in its instrument frame depends strongly on the ship's heading, represented by the yaw angle ψ. Figure 20 compares the distributions of uncorrected and post-processed high-frequency wind-direction estimates.

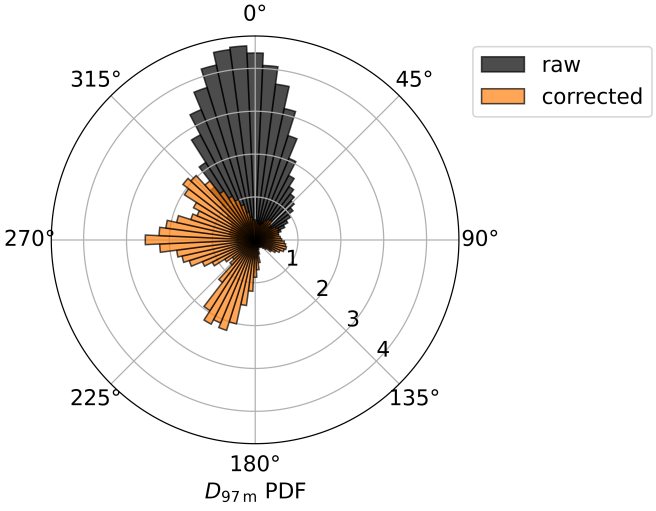


Figure 20. Probability density of high-frequency LIDAR wind-direction estimates at $h = 97\,\mathrm{m}$ during November 2021, comparing uncorrected (raw) directions in the instrument frame with motion-compensated (corrected) directions in the Earth-fixed frame.

The qualitative comparison in Section 3.2 supports the overall plausibility of the post-processed wind-direction estimates. The raw directions are concentrated around the LIDAR's nominal North direction, consistent with the moored lightship frequently orienting its bow toward the incoming wind. Because the LIDAR's internal North axis was aligned with the ship's bow, the oncoming wind translates to a measured prevailing North wind. In contrast, the corrected distribution indicates predominantly westerly winds during the investigated period. A transformation into the Earth-fixed frame is therefore required to obtain geographically referenced wind directions.

3.6.1 Yaw correction of 10-minute mean wind direction

The importance of heading correction for lightship-based wind-direction measurements was also highlighted by Cañadillas et al. (2026). Here, a simplified correction based on 10-minute averages is examined as an alternative to high-frequency motion compensation. For that, we assume that short-term variations of high-frequency D measurements due to platform tilt (i.e. pitch and roll) and translational motion are averaged out over periods of 10 minutes. Under the heading and mounting conventions used in this study, the yaw-corrected estimate is defined as

$$\overline{D}_{\mathrm{YC}} = \left(\overline{D}_{\mathrm{raw}} + \overline{\psi}\right) \bmod 360^\circ, \tag{23}$$

https://doi.org/10.5194/egusphere-2026-6846
Preprint. Discussion started: 12 November 2026
© Author(s) 2026. CC BY 4.0 License.

where $\overline{D}_{\mathrm{raw}}$ is the uncorrected 10-minute mean wind direction in the instrument frame, and $\overline{\psi}$ is the circular mean ship heading over the same interval. The result $\overline{D}_{\mathrm{YC}}$ is an estimate of the 10-minute mean wind direction in the Earth-fixed frame. The addition assumes that heading is measured clockwise from geographical North and that the LIDAR's internal North axis is aligned with the ship's bow. Circular averaging of ψ is required to account for the $0°/360°$ boundary. Wind-direction averaging must likewise account for angular wrap-around. The mean-yaw correction is an approximation when heading varies within a 10-minute interval, because adding separately averaged direction and heading is generally not equivalent to correcting individual estimates before averaging. Furthermore, although averaging can reduce the effects of fluctuating platform motion, it does not guarantee that errors associated with pitch, roll, and translational motion cancel.

Figure 21 compares the yaw-corrected estimates with the 10-minute mean directions obtained from averaging the high-frequency post-processed data, denoted $\overline{D}_{\mathrm{HF\,PP}}$, at $h = 97\,\mathrm{m}$. Table 8 summarizes their circular differences at selected measurement heights, calculated according to equation 21 with $D_2 = \overline{D}_{\mathrm{YC}}$ and $D_1 = \overline{D}_{\mathrm{HF\,PP}}$. Intervals with post-processed mean wind speeds $\overline{V}_{\mathrm{cor}} < 5\,\mathrm{m\,s^{-1}}$ or data availability below $50\,\%$ are excluded for the comparison.

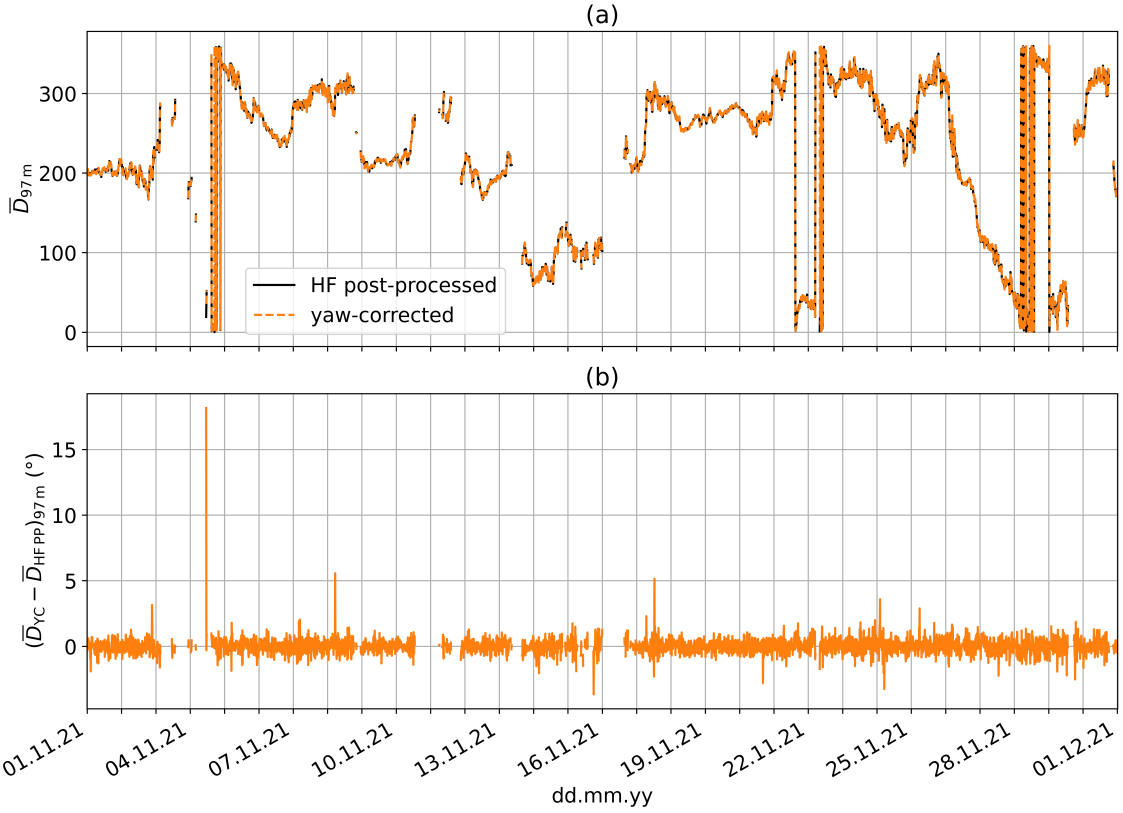


Figure 21. (a): Time series of yaw-corrected (YC) and high-frequency post-processed (HF PP) 10-minute mean LIDAR wind directions at $h = 97\,\mathrm{m}$ during November 2021. (b): Circular differences $(\overline{D}_{\mathrm{YC}} - \overline{D}_{\mathrm{HF\,PP}})$, calculated using Eq. 21. Only Intervals with post-processed mean wind speeds $\overline{V}_{\mathrm{cor}} \geq 5\,\mathrm{m\,s^{-1}}$ as well as raw and corrected data availability of at least $50\,\%$ are included.

https://doi.org/10.5194/egusphere-2026-6846
Preprint. Discussion started: 12 November 2026
© Author(s) 2026. CC BY 4.0 License.

Table 8. Summary statistics of the wrapped angular differences ($\overline{D}_{\mathrm{YC}} - \overline{D}_{\mathrm{HF\,PP}}$) between yaw-corrected and high-frequency post-processed 10-minute mean wind directions during November 2021. Differences were calculated using Eq. (21). Only intervals with post-processed mean wind speeds $\overline{V}_{\mathrm{cor}} \geq 5\ \mathrm{m\,s^{-1}}$ as well as raw and corrected data availability of at least 50 % are included. Difference statistics are reported in degrees. N denotes the number of valid data pairs.

Measurement height	Mean	Std. dev.	Min.	Max.	N
46 m	+0.009	0.651	−8.188	+14.865	3583
97 m	+0.010	0.623	−3.668	+18.154	3650
174 m	−0.012	0.703	−16.017	+13.956	3493

For the retained intervals, yaw correction agrees closely with the full motion-compensation procedure. Mean wrapped differences remain within $\pm 0.02°$, and their standard deviations are below $0.71°$ at all investigated heights. Nevertheless, individual differences reach approximately $18°$, indicating that the methods are not equivalent in every interval.

These findings support simple yaw correction as a practical alternative for obtaining geographically referenced 10-minute mean wind directions under the conditions represented by the retained dataset. Agreement between the two methods does not constitute independent validation of their absolute wind-direction accuracy. The full procedure additionally accounts for platform tilt and translational motion and provides corrected high-frequency reconstructed wind vectors. Yaw correction could also be applied to individual wind-direction estimates, but it would leave errors associated with tilt and translational motion uncorrected.

4 Discussion and conclusions

This study complements the long-term assessment of lightship-based wind-LIDAR measurements presented by Cañadillas et al. (2026), which examined operational performance and platform-motion effects over a seven-month period and included a comparison with a fixed reference LIDAR. Using data from a separate measurement period in November 2021, the present work addresses the need identified in the earlier study for improved sensor synchronization and further investigation of the correction methods. It focuses on retrospective synchronization of LIDAR and motion-sensor data, reconstruction of individual wind-vector estimates accounting for platform orientation and translational motion, and the effects of these processing steps on horizontal wind-speed estimates at different time scales and their variability as well as LIDAR-derived TI.

The SSR-based synchronization procedure yielded hourly alignment offsets ranging from $0.224\,\mathrm{s}$ to $0.590\,\mathrm{s}$, with a mean of $0.41\,\mathrm{s}$. These offsets represent the relative temporal alignment between the LIDAR and motion-sensor data that minimizes the least-squares reconstruction residuals at the nominal measurement height of $h = 97\,\mathrm{m}$; they do not provide an independent estimate of absolute timestamp accuracy. The objective function is also influenced by measurement noise, wind-field variability, and the number of valid LOS observations. Given the relatively small range of alignment offsets without any clear indication

https://doi.org/10.5194/egusphere-2026-6846
Preprint. Discussion started: 12 November 2026
© Author(s) 2026. CC BY 4.0 License.

of clock drift, a constant offset of $0.41\,\mathrm{s}$ was applied over the measurement period as a practical approximation to the hourly estimates.

Data availability was significantly reduced by post-processing at the highest three measurement heights due to the procedure of interpolating the measured radial velocities to predefined nominal heights with an integrated constant height-difference threshold. This technique is assumed to be better suited for equal spacing between nominal heights.

The effect of post-processing on the 10-minute mean horizontal wind speed was found to be small, with mean corrected-minus-raw differences ranging from $-0.037\,\mathrm{m\,s^{-1}}$ to $-0.028\,\mathrm{m\,s^{-1}}$ at the three evaluated heights. Post-processing reduced horizontal wind-speed variability, with absolute reductions in LIDAR-derived TI of approximately 0.03 in the moderate- and strong-wind categories and 0.04 in the weak-wind category. The reduction of approximately 0.03 is comparable in magnitude to the motion-related TI bias reported by Désert et al. (2021) for a buoy-mounted LIDAR. These changes demonstrate the sensitivity of LIDAR-derived turbulence statistics to the processing approach. However, the individual contributions of motion compensation and the change in wind-vector reconstruction were not separated. The reduced variability therefore does not independently demonstrate improved accuracy of the turbulence estimates, which also remain subject to limitations associated with the LIDAR's temporal and spatial sampling.

Post-processing reduced the variability of the reconstructed vertical velocity, although the distribution retained a positive mean. Without an independent reference, the contributions of atmospheric vertical motion, instrumental and setup-accuracy effects, as well as processing effects to the remaining mean and variability could not be separated.

Transforming wind vectors from the instrument frame to the Earth-fixed frame provides geographically referenced wind directions. For the investigated dataset, a simple yaw correction based on the mean platform heading yielded 10-minute mean wind directions that agreed closely with those obtained from the full motion-compensation procedure. Together with the small observed changes in 10-minute mean horizontal wind speed, this supports a simplified approach combining the original mean wind speeds with heading-corrected mean wind directions for applications focused on 10-minute mean winds under the conditions investigated. The full procedure additionally accounts for platform tilt and translation when reconstructing individual wind vectors and examining wind-speed variability.

These findings are intended to guide users of the lightship dataset in selecting processing methods appropriate to their applications and temporal scales. The present analysis compares processing approaches but does not establish a complete uncertainty budget. Full motion compensation requires valid auxiliary sensor data, so gaps in AHRS or GPS observations can prevent correction even when valid LIDAR measurements remain available. Providing the original LIDAR observations together with the available AHRS and GPS records and relevant sensor metadata would allow users to select and apply processing suited to their applications. Original LIDAR observations can be retained during auxiliary-data gaps for applications that do not require full motion compensation; geographically referenced wind direction still requires valid heading information. For future deployments, particular attention should be given to sensor calibration, time synchronization, and accurate measurement and documentation of the relative angular offsets between the LIDAR, vessel, and AHRS reference frames.

https://doi.org/10.5194/egusphere-2026-6846
Preprint. Discussion started: 12 November 2026
© Author(s) 2026. CC BY 4.0 License.

Further work could assess the sensitivity of the procedure to the uncertainty and update rate of GPS-derived platform velocities, refine the interpolation of radial velocities to predefined nominal heights, and validate the reconstructed wind statistics against independent measurements at comparable heights.

Appendix A: Thresholds for motion-data quality control

Table A1. Thresholds for motion-data quality control, i.e. range checks and step checks.

Parameter	Output frequency	Allowed range	Maximum allowed step
Pitch	10 Hz	$[-45°, 45°]$	$\pm 5°$
Roll	10 Hz	$[-45°, 45°]$	$\pm 5°$
Yaw	1 Hz	$[0°, 360°]$	$\pm 20°$
Velocity x	1 Hz	$[-10, 10]\ \mathrm{m\,s^{-1}}$	$\pm 5\ \mathrm{m\,s^{-1}}$
Velocity y	1 Hz	$[-10, 10]\ \mathrm{m\,s^{-1}}$	$\pm 5\ \mathrm{m\,s^{-1}}$
Velocity z	1 Hz	$[-5, 5]\ \mathrm{m\,s^{-1}}$	$\pm 5\ \mathrm{m\,s^{-1}}$
Δz (position offset)	1 Hz	$[-20, 20]$ m	± 5 m

Code availability. It is expected that the code used in this manuscript will be uploaded on a public repository.

Data availability. The data supporting the findings of this study are available from the corresponding author, B. Cañadillas, upon request.

Author contributions. Conceptualization, B.C.; methodology, P.G. and B.C.; measurement system design and setup, B.C.; formal analysis, P.G.; visualization, P.G.; writing—original draft preparation, P.G.; writing—review and editing, B.C. and A.L. All authors have read and agreed to the published version of the manuscript.

Competing interests. The authors declare no conflicts of interest.

Acknowledgements. This research was supported by the project "FINO-Datenbank – Erfassung und Archivierung forschungsrelevanter ozeanographischer und meteorologischer Daten auf den FINO-Plattformen", subproject "Meteorologische Messungen an FINO1" (grant number 03EE3115).

https://doi.org/10.5194/egusphere-2026-6846
Preprint. Discussion started: 12 November 2026
© Author(s) 2026. CC BY 4.0 License.

References

Benzo, C., Delbos, F., and Yahiaoui, S.: Applying motion compensation to offshore wind lidar reconstructed wind measurements, Journal of Physics: Conference Series, 2767, 042 025, https://doi.org/10.1088/1742-6596/2767/4/042025, 2024.

BSH, Bundesamt für Seeschifffahrt und Hydrographie: FINO: Forschungsplattformen in Nordsee und Ostsee, https://www.bsh.de/DE/THEMEN/Beobachtungssysteme/Messnetz-MARNET/FINO/fino_node.html, last access: 30 October 2026.

Businger, J. A.: The Marine Boundary Layer, from Air-Sea Interface to Inversion, Technischer Bericht NCAR/TN-252, National Center for Atmospheric Research, Boulder, Colorado, https://opensky.ucar.edu/system/files/2024-08/technotes_362.pdf, 1985.

Cañadillas, B., Foreman, R., Barth, V., Siedersleben, S., Lampert, A., Platis, A., Djath, B., Schulz-Stellenfleth, J., Bange, J., Emeis, S., et al.: Offshore wind farm wake recovery: Airborne measurements and its representation in engineering models, Wind Energy, 23, 1249–1265, 2020.

Cañadillas, B., Foreman, R., and Neumann, T.: Lightship-based wind-lidar measurements in the North Sea, Meteorologische Zeitschrift, p. 109541, https://doi.org/10.1127/metz/20256, 2026.

Désert, T., Knapp, G., and Aubrun, S.: Quantification and Correction of Wave-Induced Turbulence Intensity Bias for a Floating LIDAR System, Remote Sensing, 13, 2973, https://doi.org/10.3390/rs13152973, 2021.

Gottschall, J., Wolken-Möhlmann, G., Viergutz, T., and Lange, B.: Results and Conclusions of a Floating-lidar Offshore Test, Energy Procedia, 53, 156–161, https://doi.org/10.1016/j.egypro.2014.07.224, 2014.

Gutiérrez, M. A., Tiana-Alsina, J., Bischoff, O., Cateura, J., and Rocadenbosch, F.: Performance evaluation of a floating Doppler wind lidar buoy in mediterranean near-shore conditions, in: 2015 IEEE International Geoscience and Remote Sensing Symposium (IGARSS), pp. 2147–2150, ISSN 2153-7003, https://doi.org/10.1109/IGARSS.2015.7326228, iSSN: 2153-7003, 2015.

Gutiérrez-Antuñano, M. A., Tiana-Alsina, J., Salcedo, A., and Rocadenbosch, F.: Estimation of the Motion-Induced Horizontal-Wind-Speed Standard Deviation in an Offshore Doppler Lidar, Remote Sensing, 10, 2037, https://doi.org/10.3390/rs10122037, 2018.

IEC61400-50-4: Wind energy generation systems – Part 50-4: Use of floating lidar systems for wind resource assessment, https://www.iec.ch/dyn/www/f?p=103:14:0::::FSP_ORG_ID:25784, 2025.

Kelberlau, F., Neshaug, V., Lønseth, L., Bracchi, T., and Mann, J.: Taking the Motion out of Floating Lidar: Turbulence Intensity Estimates with a Continuous-Wave Wind Lidar, Remote Sensing, 12, 898, https://doi.org/10.3390/rs12050898, 2020.

Lang, S. and McKeogh, E.: LIDAR and SODAR Measurements of Wind Speed and Direction in Upland Terrain for Wind Energy Purposes, Remote Sensing, 3, 1871–1901, https://doi.org/10.3390/rs3091871, 2011.

Pauliac, R.: WINDCUBE User's manual, 2009.

Peña, A., Gryning, S.-E., and Floors, R.: Lidar observations of marine boundary-layer winds and heights: a preliminary study, Meteorologische Zeitschrift, 24, 581–589, https://doi.org/10.1127/metz/2015/0636, 2015.

Pichugina, Y. L., Banta, R. M., Brewer, W. A., Sandberg, S. P., and Hardesty, R. M.: Doppler Lidar–Based Wind-Profile Measurement System for Offshore Wind-Energy and Other Marine Boundary Layer Applications, Journal of Applied Meteorology and Climatology, 51, 327–349, https://doi.org/10.1175/JAMC-D-11-040.1, 2012.

Platis, A., Siedersleben, S. K., Bange, J., Lampert, A., Bärfuss, K., Hankers, R., Cañadillas, B., Foreman, R., Schulz-Stellenfleth, J., Djath, B., Neumann, T., and Emeis, S.: First in situ evidence of wakes in the far field behind offshore wind farms, Scientific Reports, 8, 2163, https://doi.org/10.1038/s41598-018-20389-y, 2018.

https://doi.org/10.5194/egusphere-2026-6846
Preprint. Discussion started: 12 November 2026
© Author(s) 2026. CC BY 4.0 License.



Tiana-Alsina, J., Gutiérrez, M. A., Würth, I., Puigdefábregas, J., and Rocadenbosch, F.: Motion compensation study for a floating Doppler wind LiDAR, in: 2015 IEEE International Geoscience and Remote Sensing Symposium (IGARSS), pp. 5379–5382, ISSN 2153-7003, https://doi.org/10.1109/IGARSS.2015.7327051, iSSN: 2153-7003, 2015.

TUBS, Institut für Flugführung, T. U. B.: FINO1 – Meteorologische Messungen, https://www.tu-braunschweig.de/iff/forschung/projekte/fino1-meteorologische-messungen, last access: 30 October 2026.

Yamaguchi, A. and Ishihara, T.: A new motion compensation algorithm of floating lidar system for the assessment of turbulence intensity, Journal of Physics: Conference Series, 753, 072 034, https://doi.org/10.1088/1742-6596/753/7/072034, 2016.